Photoluminescence Quenching of Organic Thin Films by Transparent Conductive Oxides

by

Jun Mei

Submitted to the Department of Materials Science and Engineering
in partial fulfillment of the requirements for the degree of

Bachelor of Science in Materials Science and Engineering

at the

MASSACHUSETTS INSTITUTE OF TECHNOLOGY

June 2006

Author .....
Department of Materials Science and Engineering
May 22, 2006

Certified by .....
Professor Vladimir Bulović
Associate Professor, KDD Career Development Chair
Thesis Supervisor

Accepted by .....
Professor Caroline Ross
Chair of the Undergraduate Committee

THIS PAGE INTENTIONALLY LEFT BLANK

Photoluminescence Quenching of Organic Thin Films by Transparent Conductive Oxides

by

Jun Mei

Submitted to the Department of Materials Science and Engineering
on May 22, 2006, in partial fulfillment of the
requirements for the degree of
Bachelor of Science in Materials Science and Engineering

Abstract

One fundamental challenge in designing organic light-emitting diodes is luminescence quenching near an electrode. In this work, we investigate the underlying mechanism behind luminescence quenching by measuring the reduction in Alq_3 photoluminescence due to SnO_2. Using an analytical model and a Monte Carlo simulation for exciton dynamics in amorphous organic solids, we find that the exciton diffusion length in bulk Alq_3 is in the range of 70–80 Å. We also find that for SnO_2 films deposited without oxygen in the sputtering ambient, resonant energy transfer from Alq_3 to SnO_2 is the dominant quenching mechanism. By varying the oxygen content in the Ar/O_2 sputtering gas mixture, we find that the energy transfer distance decreases from 10–25 Å for 0% O_2 to less than 2 Å for 10% O_2. Our experimental results suggest that because excess oxygen reduces oxygen vacancies and defect electronic states in SnO_2, it leads to a smaller spectral overlap between the emission of Alq_3 and the absorption of SnO_2, thereby shortening the energy transfer distance and reducing the quenching capability of SnO_2.

Thesis Supervisor: Professor Vladimir Bulović
Title: Associate Professor, KDD Career Development Chair

THIS PAGE INTENTIONALLY LEFT BLANK

Acknowledgments

I am indebted to everyone I have worked with since I joined LOOE in Summer 2005: I bow forever before Prof. Vladimir Bulović, my adviser, for challenging me with this project and providing invaluable guidance and support; Alexi Arango, who is like a big brother to me, for training me to use the growth systems, helping me with many measurements, and reviewing this manuscript prior to submission; M. Scott Bradley, who has been very generous with his time, patience, and expertise, for implementing the T-matrix model, which is essential to all subsequent analysis; Gerry Chen, who has been unfailingly supportive and always insightful, for assisting me in AFM and XRD measurements and critiquing various aspects of this project; Conor Madigan, who always impresses me with his encyclopedic knowledge of organic semiconductors, for indulging me with many thought-provoking discussions and providing me "the bomb," without which this thesis could not have been written. I am also grateful to Vanessa Wood for helping me with profilometry and ellipsometry, Polly Anikeeva and Steve Kooi for setting up the time-resolved measurements at ISN, John Ho and John Kymissis for showing me how to apply self-assembled monolayers to oxide substrates, Ethan Howe for fine-tuning the Monte Carlo model, and Yaakov Tischler for encouraging me from time to time. Special thanks are due to Michael Segal and Prof. Mildred Dresselhaus for granting me access to their giant electromagnet, Tim Heidel for helping me with the transmittance and reflectance measurements, David Bono from the DMSE Undergraduate Teaching Laboratory for providing technical support, and Ivan Nausieda, Jennifer Yu, Joshua Leu, and John Lock for keeping me company. Finally, I would like to thank my parents for their abiding love and life-giving belief in who I am. *Omnia meae debeo familiae.*

THIS PAGE INTENTIONALLY LEFT BLANK

Contents

List of Figures

List of Tables

THIS PAGE INTENTIONALLY LEFT BLANK

Chapter 1

Introduction

SINCE the first report of an efficient organic light-emitting diode (OLED) by Tang and VanSlyke in 1987 [1], a tremendous effort has been devoted to advancing the field of organic electronics, which offers a number of advantages over conventional silicon-based electronics. One of them is low cost. Since most organic compounds are fabric dyes or biologically derived materials [2], and they are generally processed at low temperatures, these materials can be deposited over large areas via inexpensive methods such as spin-coating [3] and ink-jet printing [3, 4]. Consequently, organic electronics can be fabricated on flexible polymer films, which is still a challenge for conventional inorganic electronics because of the high temperature deposition processes involved [5]. Today, organic electronics has become one of the most active research areas, encompassing materials engineering, device design, processes optimization, and modeling [6].

Among the most attractive research subjects within organic electronics, OLEDs hold the potential for next-generation color displays, characterized by low power consumption, high brightness, high contrast, and low cost [7–9]. Numerous companies such as Cambridge Display Technology, Universal Display, General Electric, Pioneer, Kodak, and Samsung have already begun to commercialize OLEDs; products featuring this new technology include Pioneer's OLED car stereo display, Motorola's Timeport color OLED cellular phone, Kodak's color OLED digital camera, and Samsung's E568 mobile phone. As the display technology market continues to grow at

an unprecedented rate, boasting a global market exceeding $79.9 billion in 2004 [10], more companies are expected to compete for market share with the latest technology in the near future.

Despite its astonishing progress in recent years, the OLED technology still faces a number of fundamental challenges. One important factor that restricts the performance of OLEDs is luminescence quenching—a nonradiative decay process that reduces device efficiency. Experimental and theoretical studies on the photoluminescence of organic thin films have revealed two prominent quenching mechanisms at an electrode. One is based on surface quenching at the interface [11,12] and the other on nonradiative energy transfer from the excited molecules to the electrode [13]. Combining these two nonradiative decay pathways, Burin and Ratner proposed a comprehensive model for exciton dynamics in organic thin films [14], and Wu *et al.* showed that this model can be used to extract important characteristic quantities such as the exciton diffusion length and the energy transfer distance [15].

Transparent conductive oxides are an integral part of OLEDs because their excellent charge transport properties and low absorption in the visible spectrum make them the most practical material for transparent electrodes to date. Although a number of studies have found evidence of weak photoluminescence quenching by transparent conductive oxides [16,17], so far there has not been a systematic study on this topic. The purpose of this project is to investigate photoluminescence quenching of small molecular weight organic compounds by an adjacent transparent conductive oxide film and to identify what quenching mechanism, if any, plays a dominant role. The conclusions drawn from this study may be relevant not only to OLEDs but also to other devices such as organic solar cells and photodetectors.

Chapter 2

Materials and Experimental Design

OUT of 28 million unique substances that have been identified to date,[1] this work will focus on only one particular set of materials—namely, Alq_3 and SnO_2—under the assumption that the methods we used are also applicable to other composite systems. In this chapter, we will begin with a brief introduction to the materials of interest, which is followed by a detailed description of the experimental setups and various measurement techniques.

2.1 Materials of Interest

2.1.1 Tin Oxide

Transparent conductive oxides typically exhibit wide energy bandgaps and reasonably high electrical conductivity at room temperature. Although it is not known when this class of materials was first discovered, transparent conductive oxides had found their first practical use during the World War II era, when SnO_2 coating was developed for defrosting windows in airplanes to carry out high-attitude bombing missions [18]. Chemically inert and scratch resistant [19], SnO_2 thin films are widely used today as infrared reflecting heat mirrors [18, 20], coatings for energy-conserving windows [21],

[1] According to the Chemical Abstracts Service (CAS) registry ⟨`http://www.cas.org/cgi-bin/regreport.pl`⟩, a total of 28,118,324 organic and inorganic substances have been identified as of May 21, 2006.

and transparent electrodes in optoelectronic devices [18–21].

Under typical deposition conditions, pure SnO_2 is an n-type semiconductor with a direct optical bandgap between 3.35 and 4.3 eV at room temperature and a real index of refraction between 1.8 and 2.0 in the visible spectrum [20]. As-deposited SnO_2 thin films tend to be either amorphous or nanocrystalline with tin cations arranged in octahedral coordination (rutile structure) [20, 21]. It is generally agreed that the prevailing intrinsic donor defect is oxygen vacancies, as described by the following reaction [22]

$$O_O^x \longleftrightarrow \frac{1}{2}O_2 + V_O^{\cdot\cdot} + 2e' \tag{2.1}$$

where O_O^x stands for an oxygen atom occupying a neutral oxygen site and $V_O^{\cdot\cdot}$ denotes an oxygen vacancy carrying two positive charges. Equation 2.1 suggests that under equilibrium, the population of free electrons is inversely related to that of oxygen vacancies in pure SnO_2. As shown in Appendix A, when the oxygen content—defined as the ratio of the oxygen flow rate to the total gas flow rate—in the sputtering gas mixture increases from 0 to 10% during deposition, carrier density of the as-deposited films decreases by about two orders of magnitude from $\sim 10^{20}$ to $\sim 10^{18}$ cm^{-3}.

2.1.2 Tris-(8-hydroxyquinoline) Aluminum

An important aspect in organic electronics design and engineering is the charge transport and injection properties of the organic materials, which must be chosen with close regard to their orbital energy levels. Tris-(8-hydroxyquinoline) aluminum (Alq_3) is a frequently used electron-transport and emitting material, and its electrical and optical properties have been well-characterized [23, 24]. At room temperature, the electron mobility in Alq_3 is $\sim 10^{-4}$ cm^2/V sec under an applied electric field of $\sim 10^6$ V/cm, and the hole mobility is usually at least two orders of magnitude lower [7]. As a moderately efficient luminescent material, bulk Alq_3 has a photoluminescence yield between 0.25 and 0.32 [25, 26]. The absorption and photoluminescence spectra of a typical Alq_3 thin film are plotted in Figure 2-1. The broadening in both the absorption and emission spectra arises from spatial and energy disorder of the system as

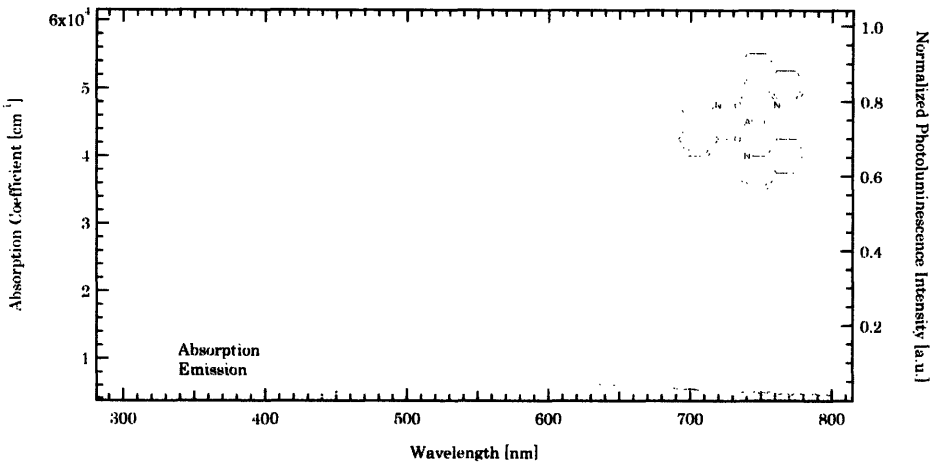

Figure 2-1: Absorption and photoluminescence spectra of a typical Alq_3 thin film, with the molecular structure shown in the inset. These broad absorption and emission spectra result from spatial and energy disorder as well as exciton-phonon coupling. The emission spectrum is red-shifted with respect to the absorption because of the Frank-Condon shift.

well as interactions between the wave functions of the excited molecules and various phonon modes. Also note that the emission spectrum is red-shifted with respect to the absorption due to the Frank-Condon shift [27]. Because the spectral overlap[2] of Alq_3 with itself is small, Alq_3 is transparent to its own radiation. Low self-absorption is another advantage that organic materials have over most inorganic semiconductors used in traditional LEDs.

2.2 Experimental Design

2.2.1 Sample Fabrication

Samples with schematic structures shown in Figure 2-2 were fabricated on 0.5×0.5 in^2 glass substrates, which were cut from 1 mm thick borosilicate glass sheets manufactured by Erie Scientific Company. Prior to device fabrication, substrates were degreased in the following order: sonication for 10 minutes in deionized water (I), 10 minutes in deionized water (II), 10 minutes in acetone, and 10 minutes in iso-

[2]Spectral overlap is defined in Chapter 3, Footnote 3.

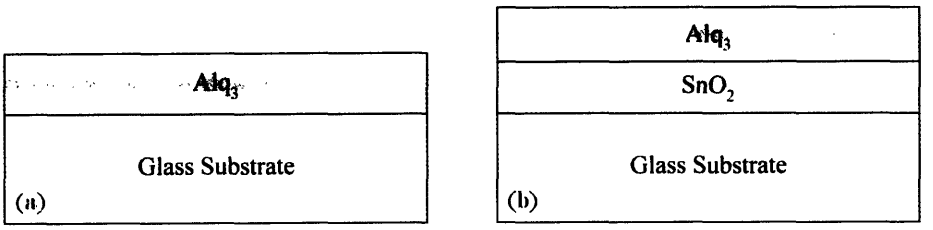

Figure 2-2: Schematic sample structures.

propanol. After cleaning, substrates were blown dry with nitrogen gas. SnO_2 films were deposited via radio frequency sputtering. The sputtering target (99.99% pure) was made by AJA International. The sputtering chamber was evacuated below 5×10^{-7} Torr prior to SnO_2 deposition. A mixture of argon and oxygen was used as the plasma-forming gas. Films of different oxygen contents were deposited by varying the oxygen flow rate while fixing the total flow rate at 10 sccm and the total pressure at 3 mTorr. Film thickness and growth rate were monitored using Sycon STM-100/MF, and the growth rate was maintained for all samples between 1.3 and 1.5 Å/sec. Alq_3 was purchased from TCI and subsequently purified by ultra-high vacuum thermal gradient sublimation [28] to achieve approximately 99% purity. Organic thin films were evaporated via Joule heating with ambient pressure below 7.0×10^{-7} Torr. The growth rate was kept the same for all samples between 1.2 and 1.6 Å/sec. Completed samples would then be stored in a nitrogen environment at room temperature with oxygen and moisture levels maintained below 1.0 ppm.

2.2.2 Photoluminescence Measurement

Certain organic materials such as Alq_3 are known to degrade quickly when exposed to oxygen and moisture [29–32]. In particular, when Alq_3 is excited in an atmospheric or oxygen ambient, it will react with oxygen and form an intermediate state that provides an efficient nonradiative decay pathway for other excited molecules [30]. Therefore, as-deposited samples must be packaged or sealed if measurements must take place in atmosphere. Nevertheless, because device packaging is a time-consuming and laborious process, it is impractical to carry out for this project. In addition, most

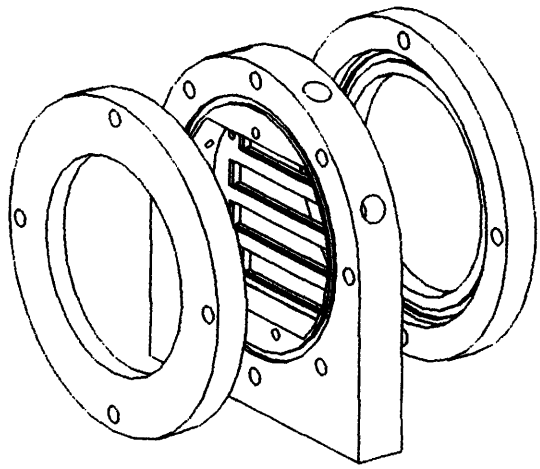

Figure 2-3: The sample chamber, also known as "the bomb," was designed by Conor Madigan to provide a nitrogen-filled airtight environment for photoluminescence measurements. This schematic diagram shows the front and back windows (both separated) as well as the sample stack, which can hold up up to 14 half-inch substrates.

epoxy used for packaging also luminesces upon excitation, thereby complicating the subsequent spectral analysis. To address these potential problems, a custom sample chamber was constructed so that samples can be placed in an airtight nitrogen environment for photoluminescence measurement. The schematic design of the sample chamber is shown in Figure 2-3.

All photoluminescence measurements were made in a configuration shown in Figure 2-4 at room temperature. Since the quantum efficiency of Alq_3 photoluminescence at the emission peak ($\lambda \simeq 525$ nm) is independent of the excitation wavelength, as dictated by Vavilov's Law [33] and experimentally confirmed for excitation wavelength between 250 and 450 nm [25], we used a Coherent Vioflame diode laser (4 mW continuous power at 408 nm) for photoexcitation. The laser spot size was narrowed by two irises arranged along the beam path, and the intensity was controlled with a continuous variable filter. All samples were excited from side with the organic/air interface. The emission was collected via optical fiber and analyzed with SpectraPro 3001 by Acton Research.

Time-resolved photoluminescence measurements were carried out at the MIT Institute for Soldier Nanotechnologies. For photoexcitation, we used a 395 nm pulse ex-

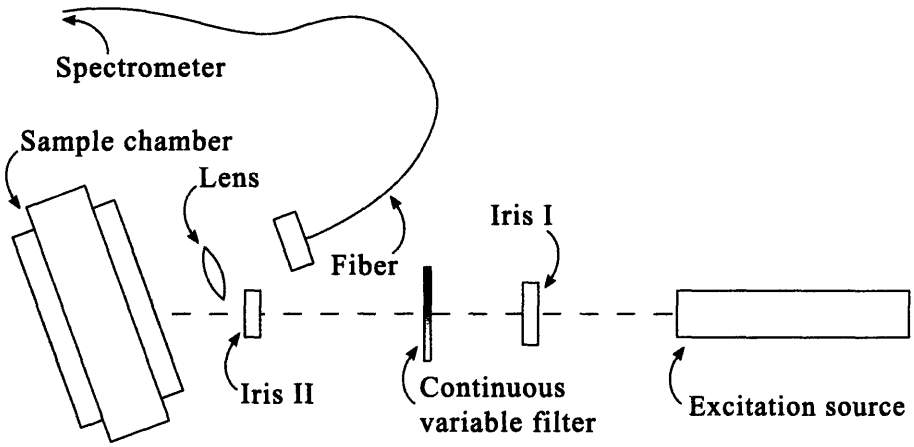

Figure 2-4: Schematic configuration for photoluminescence measurement.

citation (with pulse width less than 200 fsec) powered by a Coherent Mira 900F mode locked Ti:sapphire laser, and the intensity was modulated with a Coherent RegA 9000 regenerative amplifier. A repetition rate of 100 kHz was used for all measurements. Emitted photons were collected and analyzed using a Hamamatsu C4780 picosecond fluorescence lifetime system consisting of a Hamamatsu C4334 Streak Camera and a C5094 spectrograph. All of the measurements were integrated over 200,000 frames at a frame capture rate of 60 Hz and with a time window of 100 nsec. A typical time-resolved spectrogram is shown in Figure 2-5.

2.2.3 Other Measurements

To quantify other material properties such as the refractive index, extinction coefficient, carrier density, and crystallinity, the following measurements were performed:

- **Surface and Structural Characterization.** Rigaku 250 mm High Resolution Bragg Brettano Diffractometer was used to characterize the crystallinity of as-deposited SnO_2 films. The start and end angles (2Θ) were 20° and 80°, respectively, with an angular resolution of 0.05°. Surface morphology was characterized with atomic force microscopy (AFM) by Digital Instrument NanoScope IIIa and with profilometry by Tencor P-10 Surface Profiler.

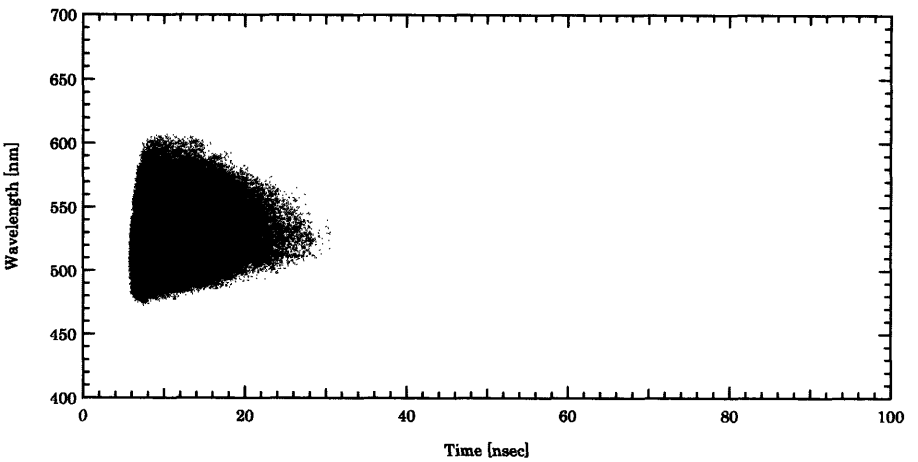

Figure 2-5: Time-resolved photoluminescence of a 400 Å thick Alq_3 thin film deposited on 600 Å thick SnO_2. In this spectrogram, color saturation reflects the intensity of emitted photons at any given wavelength and time of emission. The apparent delay in luminescence with increasing wavelength is caused by a slight misalignment of the charge-coupled device in the streak camera.

- **Optical Properties**. Transmittance and reflectance measurements were made on Cary 5E UV-Vis-NIR Spectrophotometer by Varian Analytical Instrument and Aquila nkd-8000. Geartner Ellipsometer Model L126B was used to measure the refractive index and the thickness of SnO_2 deposited on plain silicon wafer.

- **Resistivity and Hall Effect Measurements**. The van der Pauw method [34] was used extensively to calculate the resistivity, carrier density, and mobility of as-deposited SnO_2 films. Samples were probed with a Keithley Model 2420 High-Current SourceMeter and a Model 2602 Dual-Channel System SourceMeter under 4-wire mode. For Hall-coefficient measurements, we used an electromagnet (kindly provided by Prof. Dresselhaus) to generate a magnetic field of 4.4 ± 0.1 kG [35] normal to the sample surface.

THIS PAGE INTENTIONALLY LEFT BLANK

Chapter 3

Model for Exciton Dynamics

EXCITON dynamics in organic solids is fundamental to all organic electronics. In this chapter, we will present a simple model for exciton dynamics in organic thin films. The goal of this study is to understand how excitons behave in an amorphous organic solid given a number of concurrent processes, such as exciton generation, decay, migration, resonant energy transfer, and interfacial quenching.

3.1 Overview

Excitons are mobile excited states that can be generated from photoexcitation, carrier recombination, electrochemiluminescence, thermal or chemical activation, or even interactions between excitons [36]. In this work, we are concerned with photoexcitation only, in which ground state electrons are promoted to higher energy states by absorbing passing photons. Once an exciton is formed, it can be classified into one of the following types: Wannier-Mott, Frenkel, or charge-transfer. If there is a significant orbital overlap among neighboring molecules, then the electron-hole pair associated with an exciton can be delocalized over the surrounding molecules due to strong intermolecular interactions. These excited species are known as Wannier-Mott excitons, which can be modeled by hydrogen-like wave functions with a large mean electron-hole distance (40–100 Å) [36, 37]. Wannier-Mott excitons are common in inorganic crystals such as high quality Si, Ge, and LiH [27, 38], but much less likely

(a) Frenkel Exciton **(b) Wannier-Mott Exciton**

Figure 3-1: Schematic diagrams of (a) a Frenkel exciton and (b) a Wannier-Mott exciton. This figure is adopted from Bulović *et al.* (2001).

to be found in molecular solids bounded by van der Waals forces. On the other hand, if the binding energy is strong ($\gg kT$), then the electron-hole pair will be localized on the same molecule, forming an excited species known as the Frenkel exciton, with a typical radius of ~5 Å [2, 36, 37]. Schematic diagrams of a Frenkel exciton and a Wannier-Mott exciton are shown in Figure 3-1. Between these two extremes is an intermediate state called the charge-transfer exciton in which the electron-hole pair is neither extended too far nor bound to any particular site. Both Frenkel and charge-transfer excitons are typical of organic solids.

To model how excitons are distributed in an amorphous organic solid, let $N(\mathbf{r}, t)$ denote the exciton population density at position $\mathbf{r}$ and time t. Then the time-dependent distribution of excitons is given by

$$\frac{\partial N(\mathbf{r},t)}{\partial t} = \left.\frac{\partial N(\mathbf{r},t)}{\partial t}\right|_{\text{mig}} + \left.\frac{\partial N(\mathbf{r},t)}{\partial t}\right|_{\text{dec}} + \left.\frac{\partial N(\mathbf{r},t)}{\partial t}\right|_{\text{gen}} + \left.\frac{\partial N(\mathbf{r},t)}{\partial t}\right|_{\text{other}} \tag{3.1}$$

This general expression assumes a number of concurrent and independent processes which are identified as exciton generation, migration, decay, and others. In this work, we assume that other processes have negligible effects on the population distribution. Thus, Equation 3.1 can be recast as

$$\frac{\partial N(\mathbf{r},t)}{\partial t} = \left.\frac{\partial N(\mathbf{r},t)}{\partial t}\right|_{\text{mig}} + \left.\frac{\partial N(\mathbf{r},t)}{\partial t}\right|_{\text{dec}} + \left.\frac{\partial N(\mathbf{r},t)}{\partial t}\right|_{\text{gen}} \tag{3.2}$$

For completeness, different types of interfacial reactions will be formulated in terms of the boundary conditions imposed on Equation 3.2.

3.2 Physical Model

3.2.1 Exciton Generation

In this model, we assume that the dominant exciton generation process is photoexcitation. This assumption is valid because for all photoluminescence measurements carried out in this work, neither chemical excitation nor charge injection is likely to occur in an isolated and inert environment, such as our nitrogen-filled sample chamber. Furthermore, at room temperature, thermal energy on the order of $kT = 0.026$ eV is not sufficient to promote electrons from the highest occupied molecular orbital of Alq_3 across an energy gap of ~2.7 eV [23] to the lowest unoccupied molecular orbital. Therefore, the only excitation mechanism that we will consider is photoexcitation.

Given a steady influx of photons, the rate at which excitons are generated should be independent of time. Thus, we write

$$\left.\frac{\partial N(\mathbf{r},t)}{\partial t}\right|_{\text{gen}} = G(\mathbf{r}) \tag{3.3}$$

In general, when light passes through a uniform material of some thickness d, the fraction of incident photons emerged from the sample is determined by the Beer-Lambert law,[1] given by [33]

$$I(d) = I_0 e^{-\alpha d} \tag{3.4}$$

where I_0 is the initial intensity and α the absorption coefficient of the medium. The absorption coefficient is related to the imaginary part of the complex refractive index $\tilde{n}$ (where $\tilde{n} = n + \jmath\kappa$) by $\alpha = 4\pi\kappa/\lambda$. At $\lambda = 408$ nm, the absorption coefficient of Alq_3 is found to be approximately 5.6×10^4 cm^{-1}.

For an optically thin film with $d \ll \alpha^{-1}$, only a small fraction of the incident pho-

[1] Also known as Beer's law or the Beer-Lambert-Bouguer law.

tons are absorbed upon the first pass. Thus, photons reflected from the substrate/air interface will also contribute to exciton generation.[2] Moreover, if the medium does not completely dephase incident light, then reflections from multiple interfaces may even interfere with one another and experience a weak microcavity effect, thereby further complicating the photoexcitation process. To address these issues, we have developed an optical model based on T-matrices to predict the amount of incident power absorbed by the organic layer. Details of the model are discussed in Appendix B. Although its predictions match the results from transmission measurements, our optical model is unable to trace the excitation power distribution within the absorbing layer. Therefore, to the extent that the samples are optically thin, we assume a uniform generation rate $G(\mathbf{r}) = \zeta$, where ζ is calculated from T-matrices.

3.2.2 Exciton Decay

Over time, excited molecules will relax and return to their ground states either radiatively or nonradiatively. In a radiative transition, an electron-hole pair recombines and emits a photon, and there are two ways by which this process can take place: fluorescence and phosphorescence. Fluorescence is a fast radiative process in which the spin multiplicities are preserved (e.g. singlet-singlet transitions) as the excited molecule relaxes. The rate constant is typically in the range between $\sim 10^6$ and $\sim 10^9$ sec^{-1} [27]. In phosphorescence, the spin multiplicities are not preserved (e.g. triplet-singlet transitions). For most systems, this process requires a strong spin-orbit coupling in which the phosphorescent dipole moment is pulled toward the fluorescent dipole moment. Consequently, phosphorescence is a much slower process with a typical rate constant in the range between $\sim 10^{-2}$ and $\sim 10^6$ sec^{-1} [27], and it is observable mainly in the presence of a heavy element such as Pt or Ir, near which spin-orbit coupling is greatly enhanced [41].

[2] Fresnel's formulas specify the reflectance and transmittance for perpendicular incidence of light at an interface [39, 40],

$$R = \left(\frac{p-1}{p+1}\right)^2 \quad . \quad T = \frac{4p}{(p+1)^2}$$

where $p = n_1/n_2$ is the ratio of the refractive index on one side of the interface to the other.

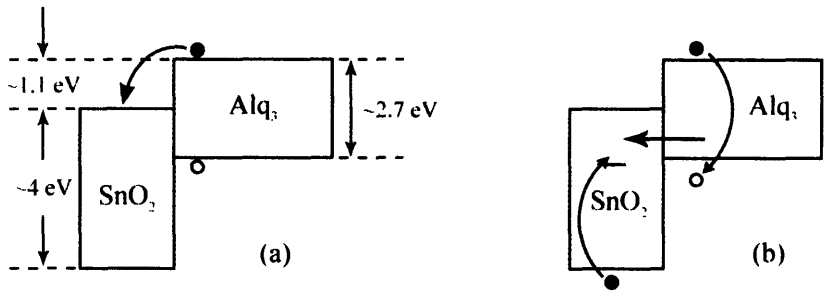

Figure 3-2: Band diagrams illustrating two possible quenching mechanisms: (a) exciton dissociation at the Alq_3/SnO_2 interface and (b) energy transfer from Alq_3 to SnO_2.

Nonradiative transitions occur in a number of ways. For example, energy can be dissipated through lattice vibrations or molecular collisions that are facilitated by exciton-phonon coupling. The rate constant associated with this process can be as high as $\sim 10^{12}$ sec^{-1} [27,36]. Interactions among excitons can also lead to nonradiative decay in a process known as exciton-exciton annihilation, which is observable at high exciton concentrations [42,43]. Additionally, impurities and defects can provide efficient quenching sites for all excitons nearby. In particular, when an exciton reaches an interface that has a lower energy level, such as the Alq_3/SnO_2 interface shown in Figure 3-2a, the electron-hole pair can dissociate into completely separate charge carriers. Furthermore, if the SnO_2 layer contains a large number of bandgap states, free carriers, or both, such that it responds to the radiative dipole field of an excited molecule, then when an exciton is sufficiently close to the Alq_3/SnO_2 interface, the exciton can transfer its energy nonradiatively to SnO_2 (Figure 3-2b). Despite these different types of nonradiative decay processes, only surface quenching and resonant energy transfer from Alq_3 to SnO_2 are not completely intrinsic to Alq_3. Thus, the main quenching mechanisms we will consider in this study are surface quenching and energy transfer.

Combining both radiative and nonradiative transitions, we obtain a general expression for exciton decay:

$$\left.\frac{\partial N(x,t)}{\partial t}\right|_{\text{dec}} = -\frac{N(x,t)}{\tau} \tag{3.5}$$

where $1/\tau$ is the total decay rate given by

$$\frac{1}{\tau} = \frac{1}{\tau_{\mathrm{r}}} + \frac{1}{\tau_{\mathrm{nr}}} \tag{3.6}$$

By convention, τ is called the exciton lifetime, and the ratio of the radiative rate to the total decay rate is called the photoluminescence yield ($\phi \equiv \tau/\tau_{\mathrm{r}}$), which measures the probability that an average exciton decays radiatively at any moment should it choose to relax. For pure Alq_3 thin films, the exciton lifetime reported in literature varies from 12 to 17 nsec [26, 44, 45] and the photoluminescence yield from 25 to 32% [25,26]. Both τ and ϕ can be modified by selective doping. For instance, when a host molecule is excited near an absorbing layer or particle,[3] the excited molecule can transfer its energy to the acceptor through dipole-dipole interactions (Förster energy transfer) [46] or electron exchange (Dexter energy transfer) [47]. If the acceptor has a much faster nonradiative relaxation rate than the energy transfer rate from the acceptor back to the donor, then the acceptor becomes an effective exciton quencher, which drastically reduces τ and suppresses ϕ.

It has been reported that the presence of a metal electrode in contact with a thin fluorescent film facilitates short-distance energy transfer from the fluorescent layer to the metal [11–13, 15, 48–50]. This process occurs when the short-range dipole field of an exciton strongly couples with the plasmon modes of the two-dimensional electron gas present at the interface between the organic layer and the metal electrode [50]. Kuhn showed that the relationship between the lifetime of a dipole emitter and its distance x from the surface of a thin absorbing layer can be approximated as

$$\frac{1}{\tau} = \frac{1}{\tau_\infty}\left[1 + \theta_4\left(\frac{\lambda}{4\pi n x}\right)^4 + \theta_2\left(\frac{\lambda}{4\pi n x}\right)^2\right] \tag{3.7}$$

[3]Material A is absorbing with respect to B if there is a significant spectral overlap between the two. The spectral overlap is given by

$$I = \int_0^\infty \alpha_{\mathrm{A}}(\lambda) f_{\mathrm{B}}(\lambda) \lambda^4 d\lambda$$

where $\alpha_{\mathrm{A}}(\lambda)$ is the molar absorption spectrum of A and $f_{\mathrm{B}}(\lambda)$ the area-normalized emission spectrum of B [46].

where τ_∞ is the exciton lifetime in the absence of the absorbing layer, λ the emission wavelength, n the refractive index of the emitting layer, and $\theta_{2,4}$ steric factors determined by the orientation of the exciton dipole moment [51, 52].

For an absorbing layer of finite thickness, we need to integrate the energy transfer terms in Equation 3.7 over the thickness of the absorbing layer. Before we proceed, we shall make an additional simplification: As the emission spectrum of Alq_3 peaks at $\lambda \simeq 525$ nm, for organic films thinner than 100 nm, the quartic term in Equation 3.7 dominates, i.e. $(\lambda/x)^4 \gg (\lambda/x)^2$, and this has been experimentally observed in many cases [51–53]. Thus, neglecting the quadratic term, we integrate the energy transfer rate in Equation 3.7 over the thickness of the absorbing layer and obtain the following expression:

$$\frac{1}{\tau} = \frac{1}{\tau_\infty}\left[1 + \left(\frac{x_0}{x}\right)^3\right] \tag{3.8}$$

where x_0 is the distance at which the probability that an exciton decays at the host molecule is equal to the probability that it transfers its energy to the absorbing layer, analogous to the Förster radius.[4] Based on a classical approach, Chance *et al.* derived a general expression for x_0 [13]

$$x_0^3 = \frac{3\phi}{32}\frac{\lambda^3\Theta}{\pi^3 n_1}\left[\frac{n_2\kappa_2}{(n_1^2 + n_2^2 - \kappa_2^2)^2 + 4n_2^2\kappa_2^2}\right] \tag{3.9}$$

where ϕ is the photoluminescence yield, n_1 the real refractive index of the host medium, n_2 and κ_2 the real and imaginary parts of the complex refractive index

[4] Based on an equilibrium Fermi Golden Rule approach. Förster found that the rate of energy transfer for coupling of a state to a quasi-continuum of secondary states is

$$k = \frac{\phi}{\tau}\left(\frac{R_0}{R}\right)^6$$

where R is the separation between the donor and the acceptor, and R_0 is known as the Förster radius, which is determined by:

$$R_0^6 = \frac{8.785 \times 10^{-25}\ [\text{M cm}^3]\ I}{n^4}$$

where n is the refractive index of the medium and I the spectral overlap defined in Footnote 3, assuming that I has units of M^{-1}cm^3 [46]. In pure Alq_3 thin films, for example, one would find that the Förster radius between Alq_3 molecules is about 11 Å [2]. This small radius is a direct result of the low self-absorption of Alq_3.

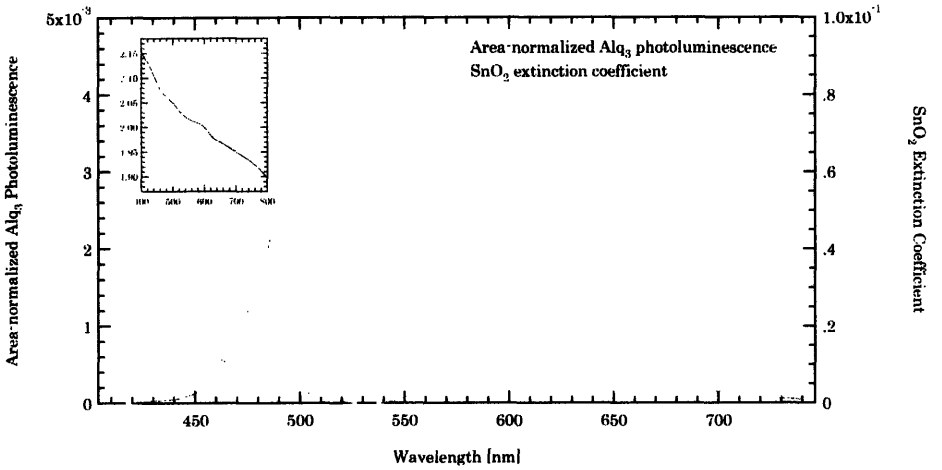

Figure 3-3: Spectral overlap of the area-normalized emission of Alq_3 and the extinction coefficient of SnO_2 with the real refractive index shown in the inset. The complex refractive index of SnO_2 is taken from Martín-Palma and Martínez-Duart (1998).

of the acceptor, and Θ a geometry factor for the different dipole orientations with respect to the absorbing layer (2 for a vertical dipole and 1 for a horizontal dipole). Equation 3.9, however, applies only to narrow-band emissions centered at λ. For broad-band emission materials such as Alq_3, it should be rewritten in a fashion that integrates over the entire emission spectrum of the exciton:

$$x_0^3 = \frac{3\phi}{32}\frac{\Theta}{\pi^3}\int_0^\infty \frac{n_2\kappa_2 f(\lambda)}{(n_1^2+n_2^2-\kappa_2^2)^2+4n_2^2\kappa_2^2}\frac{\lambda^3}{n_1}d\lambda \tag{3.10}$$

which is similar to the Förster radius formulated in Footnote 4.

As a first approximation, if we assume that the real refractive index of Alq_3 is $n = 1.70$ [45] and constant for all λ, the area-normalized emission spectrum $f(\lambda)$ as determined by this work, the complex refractive index of pure SnO_2 as reported in Reference 54, the photoluminescence yield $\phi = 0.32$ [25], and $\Theta = 4/3$ for a randomly orientated dipole [14], then according to Equation 3.10, by integrating λ from 400 to 800 nm, the energy transfer distance from Alq_3 to SnO_2 is found to be 32 Å.

We note that the preceding calculation is a rough estimation of the energy transfer distance. Because our SnO_2 deposition conditions differ from those used by Martín-Palma and Martínez-Duart, it is unlikely that our SnO_2 films have the same refractive

index reported in Reference 54. Since SnO_2 is a weak absorber ($\kappa < 0.1$) in the visible spectrum, κ can vary by a factor of 2 to 5 depending the deposition conditions while n remains relatively constant ($n \simeq 1.8$–2.0). Thus, the actual energy transfer distance can differ from the calculated value by as much as 50%, but the upper bound is unlikely to exceed $2 \times 32 \simeq 60$ Å, which is close to those of metals and other highly absorptive materials.

3.2.3 Exciton Migration

Within its lifetime, an exciton can migrate from one molecular site to another due to intermolecular interactions. In the weak-coupling limit (as in Wannier-Mott excitons), excitons with well-defined momentum $\mathbf{p} = \hbar\mathbf{k}$ are formed, and they move in a wave-like (or coherent) manner [55]. Because of the large exciton-phonon interactions in organic materials, the time in which excitons remain coherent is short, typically less than 10^{-13} sec at room temperature [36]. For Frenkel excitons, the wave vector $\mathbf{k}$ is no longer a good quantum number, and excitons move incoherently in a random hopping-like manner [55]. Given that the lifetime of excitons in organic materials is normally on the order of nanoseconds, excitons migrate predominately by hopping to neighboring sites. Since the size of an Alq_3 molecule is ~8 Å [56], and the Förster radius between Alq_3 molecules is ~11 Å [2], Förster energy transfer facilitates exciton migration in Alq_3 [45]. Although Dexter energy transfer can also contribute to exciton migration, the rate associated with correlated electron exchange between two molecules is usually much slower than the Förster energy transfer rate in pure Alq_3 solids [45]. For a more detailed review on exciton diffusion, readers are referred to Reference 57.

To the extent that a vast majority of excitons move by hopping, we can treat them as classical particles diffusing through a solid. Suppose an exciton is formed at position $\mathbf{r}_i$ and it hops about until it vanishes at $\mathbf{r}_f$, then the average linear displacement $\langle|\mathbf{r}_f - \mathbf{r}_i|\rangle$ is called the exciton diffusion length or L_d. Obviously, the total distance traveled in a random walk is expected to be much greater than the linear displacement between the initial and final positions. In fact, it can be shown that in an isotropic structure with a lattice constant Λ, if an exciton is allowed to hop

to its nearest neighbor only, then the total distance traveled during its lifetime is approximately L_d^2/Λ [36].

To model exciton diffusion in an amorphous organic film, we adopt the classical approach by assuming that there is a continuum of available sites. Assuming that the diffusion process obeys Fick's Second Law, we get

$$\left.\frac{\partial N(\mathbf{r},t)}{\partial t}\right|_{\text{diff}} = D\frac{\partial^2 N(\mathbf{r},t)}{\partial \mathbf{r}^2} \tag{3.11}$$

where D is the diffusion constant. Although Equation 3.11 allows for a simple reconstruction of exciton diffusion in an amorphous solid by collapsing both the spatial and energy disorder into a single parameter D, it is not useful for analyzing many intricate properties of organic solids, for which discrete modeling from a first-principle approach is more appropriate. Nevertheless, discrete modeling is beyond the scope of this work. For relevant information regarding discrete modeling, readers are referred to Reference 45 and 58.

3.3 Analytical Solutions

3.3.1 Steady State

Assuming that the system reaches steady state, we obtain the following expression by incorporating exciton generation, decay, and diffusion into Equation 3.2:

$$\frac{\partial N(\mathbf{r},t)}{\partial t} = D\frac{d^2 N(\mathbf{r})}{d\mathbf{r}^2} - \frac{N(\mathbf{r})}{\tau_\infty}\left[1+\left(\frac{x_0}{x}\right)^3\right] + G(\mathbf{r}) = 0 \tag{3.12}$$

By symmetry, we deduce that exciton density depends only on the distance in the direction normal to the quenching surface. Since we have implicitly defined the $\hat{y}$ and $\hat{z}$ directions to be parallel to the surface, after rearranging the coefficients in Equation 3.12, we get

$$\frac{d^2 N(x)}{dx^2} - \frac{N(x)}{L_d^2}\left(1+\frac{x_0^3}{x^3}\right) + g(x) = 0 \tag{3.13}$$

where $L_d = \sqrt{D\tau_\infty}$ is the normal diffusion length for excitons in bulk materials without any extrinsic decay mechanism. We note that a more precise definition should be $L_d = \sqrt{ZD\tau_\infty}$, where $Z = 2$ for strictly one-dimensional diffusion, 4 for two-dimensional diffusion, and 6 for three-dimensional diffusion [36,44]. But in literature, Z is usually taken for unity. Therefore, we shall follow the same convention.

3.3.2 Surface Reactions and Boundary Conditions

Since the general solution to Equation 3.13 is not known, to obtain the analytical solutions, we have developed a numerical solver[5] specifically for the following boundary conditions:

1. **No surface quenching**. If excitons do not dissociate or recombine at the organic/inorganic interface, then they will have to diffuse back into the organic film. In this case, the net flow at interface is zero, and similar conditions also hold at the organic/air interface:

$$\left.\frac{dN(x)}{dx}\right|_{x\to 0} = 0 \quad , \quad \left.\frac{dN(x)}{dx}\right|_{x\to d} = 0 \tag{3.14}$$

2. **Partial quencher**. We assume that the organic/air interface remains inert, but at the inorganic/organic interface, excitons are quenched at a finite velocity v. Thus, by the conservation of mass, we get

$$\left.D\frac{dN(x)}{dx}\right|_{x\to 0} = \lim_{x\to 0} vN(x) \quad , \quad \left.\frac{dN(x)}{dx}\right|_{x\to d} = 0 \tag{3.15}$$

3. **Perfect quencher**. The organic/air interface is assumed to be inert. A perfect quencher causes excitons to decay immediately by dissociation or recombination when they reach the quenching surface. Consequently, the population density at the quenching surface is zero. Hence,

$$\lim_{x\to 0} N(x) = 0 \quad , \quad \left.\frac{dN(x)}{dx}\right|_{x\to d} = 0 \tag{3.16}$$

[5]The Matlab script for the numerical solver is attached in Appendix C.

3.4 Monte Carlo Simulation

To further our understanding of exciton dynamics in organic solids, we have implemented a Monte Carlo model to simulate the time evolution of excitons in organic thin films.[6] The assumptions for this model are:

1. There is a continuum of available sites, and excitons are generated randomly in space with a uniform distribution, which is valid for optically thin films.

2. Excitons can get arbitrarily close to one another or even occupy the same site without triggering exciton-exciton annihilation.

3. Exciton dynamics is modeled one time step per cycle. In each time step Δt, an exciton chooses to decay with probability $1 - \exp(-\Delta t/\tau)$, where τ is given by Equation 3.8. If the exciton decays, it will emit a photon with probability $1/(1+x_0^3/x^3)$, and the time of emission is recorded. By making this assumption, we ignore a number of secondary effects. For example, it was recently shown that the mean emission spectrum of Alq_3 shifts to lower energies with increasing time [45]. Thus, the probability that an exciton emits at one particular wavelength is different from another. On the other hand, since the energy shift is small ($\sim$0.04 eV or $\sim$10 nm), it is still valid to assume that the emission probability is invariant with wavelength.

4. If relaxation does not occur, the exciton will migrate to a different site. Diffusion is strictly one-dimensional, and the displacement is randomly chosen with a zero-mean normal distribution, which assumes that exciton diffusion is a random walk process. It can be shown that the standard deviation L scales with the exciton diffusion length by $L = L_d\sqrt{\Delta t/\tau_\infty}$.

5. At the two boundaries, if the exciton hits the air/organic interface, it will bounce back. Otherwise, it will be annihilated with probability p.

Repeating the preceding process over a large number of cycles, we obtain a histogram of the emission intensity against time.

[6]The Matlab script is attached in Appendix D.

3.5 Summary

A physical model for exciton dynamics in organic solids has been described with close regard to exciton generation, decay, and migration. Using a classical approach, we have derived a general expression for the steady state distribution of excitons in an organic thin film. With a similar approach, we have also designed a Monte Carlo model to simulate the time evolution of excitons. We will apply these methods to analyze experimental results in the next chapter.

THIS PAGE INTENTIONALLY LEFT BLANK

Chapter 4

Experimental Results

IN the preceding chapter, we described an analytical model and a Monte Carlo model for exciton dynamics in organic solids, given a number of concurrent and independent processes such as exciton generation, decay, migration, surface quenching, and resonant energy transfer. In this chapter, these models will be applied to analyze experimental results.

4.1 Steady State Photoluminescence

To test our models, we deposited Alq_3 thin films with thickness ranging from 10 to 700 A on 600 Å thick SnO_2 substrates[1] and measured their time-integrated photoluminescence under steady state. Normalized emission spectra of these samples are plotted in Figure 4-1a, which shows that the emission peaks of these samples center at $\lambda \simeq 523 \pm 3$ nm. Although the spectral width of the emission peak narrows with increasing Alq_3 thickness, it is probably due to an improved signal-to-noise ratio with thicker fluorescent films. Therefore, there is no indication of microcavity or optical interference effects that can potentially shift the emission peak or narrow the spectral width.

The relative peak intensity of each sample is plotted in Figure 4-1b, which shows a significant depression in the photoluminescence of Alq_3 films with thickness less than

[1] SnO_2 was sputtered onto glass substrates with only Ar (0% O_2) in the sputtering ambient.

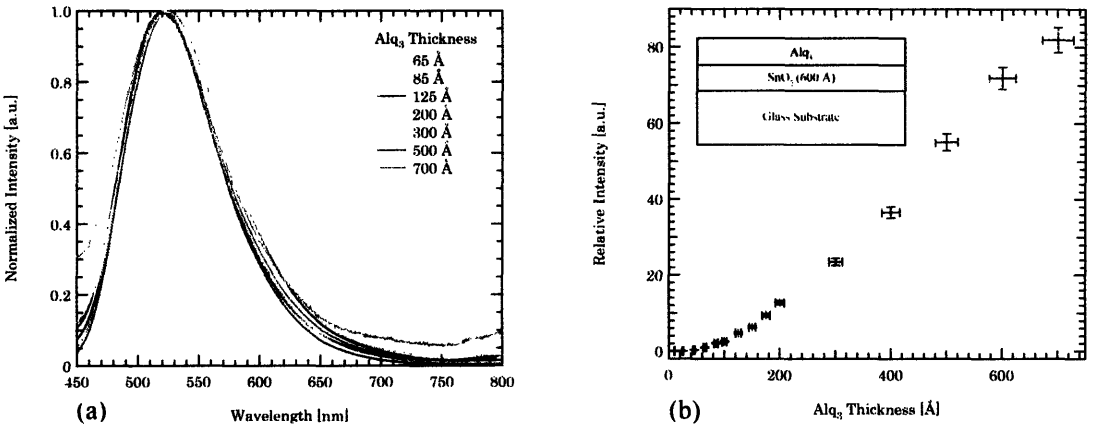

Figure 4-1: Photoluminescence of Alq_3 thin films on SnO_2 substrates: (a) normalized emission spectra and (b) relative peak intensity as a function of film thickness. The sample structure is drawn in the inset of (b).

200 Å. From Figure 4-1b, it is evident that SnO_2 quenches the photoluminescence of Alq_3. To relate the analytical model to the experimental results, we need to calculate the photoluminescence quantum efficiency of each sample. The photoluminescence quantum efficiency is defined as $\eta \equiv F/A$, where A is the number of photons absorbed and F the number of photons emitted. Based on our analytical model, both $A(d)$ and $F(d)$ of an organic film with thickness d can be computed directly:

$$A(d) = \int_0^d G(x)dx \quad , \quad F(d) = \int_0^d \frac{N(x)}{\tau_r}dx \tag{4.1}$$

As for the experimental results, we assume that the absorption in Alq_3 follows the Beer-Lambert law given by Equation 3.4, which allows us to calculate the relative photoluminescence efficiency for each sample at the emission peak.

In Figure 4-2, we compare the relative photoluminescence efficiency calculated from the experimental results with the best theoretical fit from our analytical model given different boundary conditions. A best theoretical fit to the experimental results is obtained by optimizing the input parameters (e.g. L_d, x_0, and v) and an additional scaling factor so that the sum of squared fitting error is minimized. We have examined three principal models, namely, (1) a perfect quenching surface with no energy

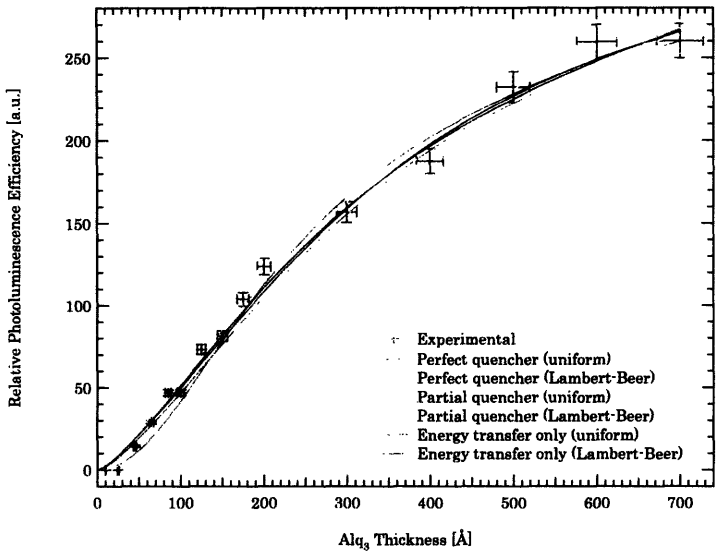

Figure 4-2: Relative photoluminescence efficiency of Alq_3 thin films and theoretical fittings: (1) a perfect quenching surface with no energy transfer, (2) a partial quenching surface with no energy transfer, and (3) energy transfer only. For each model, both uniform and Lambert-Beer exciton generations are also considered.

transfer, (2) a partial quenching surface with no energy transfer, and (3) quenching by energy transfer only. Although there are two other possible combinations, i.e. (i) a perfect quenching surface with energy transfer and (ii) a partial quenching surface with energy transfer, we find that the former always converges to a perfect quenching surface with no energy transfer (i.e. $x_0 \rightarrow 0$) after optimization. As to the latter, because of its complexity, experimental errors introduced by instrumental limitations and background noise are probably too large for our model to accurately resolve every input parameter. Thus, only the three simpler models are considered for subsequent analysis.

In Table 4.1, we tabulate the input parameters for each theoretical fit. Overall, models that assume either a finite surface recombination velocity or a small energy transfer distance fit better with the experimental results. The exciton diffusion length extracted from these models ranges from 136 ± 10 Å for the perfect quenching surface case with uniform exciton generation rate to 251 Å for the energy transfer only case with Lambert-Beer exciton generation rate. Despite this wide range, the upper and

PERFECT QUENCHER WITHOUT ENERGY TRANSFER

Exciton Generation	Best Fit Parameter(s)	Fitting Error
Uniform	$L_d = 136.4 \pm 9.7$ Å	26.35
Lambert-Beer	$\alpha = 5.6 \times 10^4$ cm^{-1} (fixed) $L_d = 162.0 \pm 22.6$ Å	28.54

PARTIAL QUENCHER WITHOUT ENERGY TRANSFER

Exciton Generation	Best Fit Parameter(s)	Fitting Error
Uniform	$\tau = 17.4$ nsec (fixed) $L_d = 192.4 \pm 62.3$ Å $v = 42.0 \pm 28.7$ Å/nsec	23.05
Lambert-Beer	$\tau = 17.4$ nsec (fixed) $\alpha = 5.6 \times 10^4$ cm^{-1} (fixed) $L_d = 237.3 \pm 140.0$ Å $v = 49.93$ Å/nsec (optimal)	20.09

ENERGY TRANSFER ONLY

Exciton Generation	Best Fit Parameter(s)	Fitting Error
Uniform	$L_d = 200$ Å (optimal) $x_0 = 1.5$ Å (optimal)	23.06
Lambert-Beer	$\alpha = 5.6 \times 10^4$ cm^{-1} (fixed) $L_d = 251$ Å (optimal) $x_0 = 1.6$ Å (optimal)	19.93

Table 4.1: Comparison of different models: The input parameters are denoted by L_d (exciton diffusion length), α (Alq_3 absorption coefficient at 408 nm), τ (exciton lifetime), v (surface recombination velocity), and x_0 (energy transfer distance).

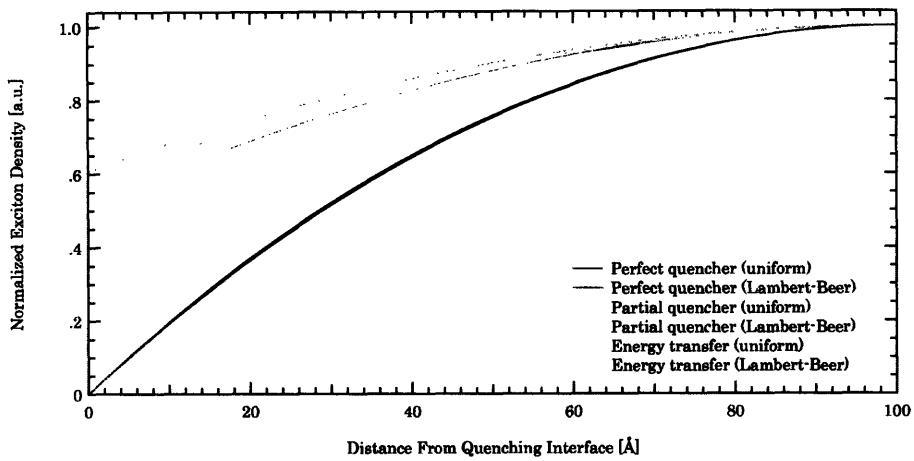

Figure 4-3: Steady state exciton population density of a 100 Å thick Alq_3 film on SnO_2 calculated using different distribution models.

lower bounds are within those values reported in literature, varying from ~80 Å [15,59] to ~290 Å [14], for which similar analysis was performed.

It is interesting to note that the energy transfer distance extracted from the best theoretical fit (1.5 Å for uniform generation and 1.6 Å for Lambert-Beer generation rate) is much shorter than we previously estimated (~30 Å), and if we fix the energy transfer distance at 32 Å, the resulting error is found to be as large as the perfect quencher case without energy transfer. In Figure 4-3, we plot the normalized steady state exciton population density in a 100 Å thick Alq_3 layer calculated from each model using the parameters listed in Table 4.1. It shows that when the energy transfer distance is much shorter than the exciton diffusion length, the energy transfer process becomes indistinguishable from surface quenching with a finite velocity.

Extracted from the best theoretical fit, the surface quenching velocity is found to be 42.0 ± 28.7 Å/nsec for uniform exciton generation and 49.9 Å/nsec for Lambert-Beer generation. Comparing these values to those reported by Gregg *et al.*, who investigated photoluminescence quenching of polymer films deposited on SnO_2, we find that the quenching velocity extracted from our experimental results is about one order of magnitude lower than the reported value of 600 Å/nsec [16]. Nevertheless, because the surface quenching velocity is material dependent and is strongly influ-

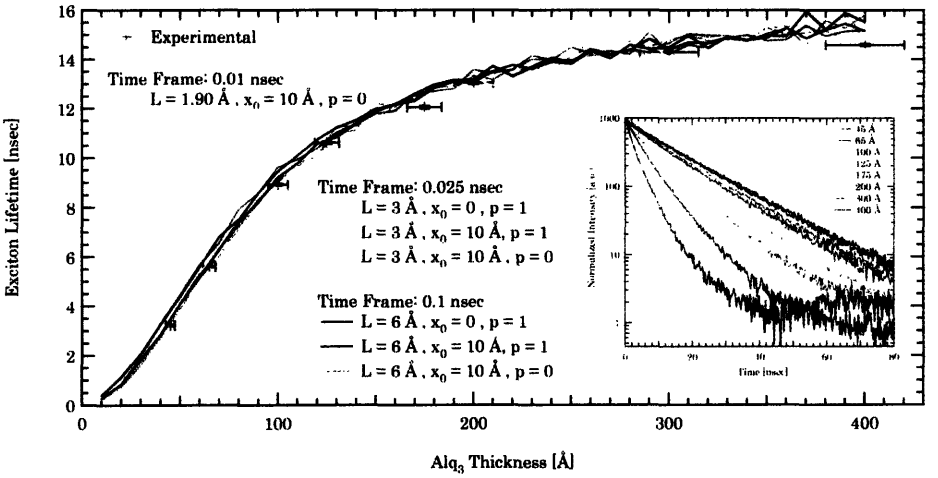

Figure 4-4: Comparison between experimental and simulation results: Exciton lifetime is plotted against Alq_3 film thickness. Time-resolved photoluminescence of Alq_3 with various film thickness on 600 Å SnO_2 (0% O_2) is shown in the inset. Input parameters are denoted by L (standard deviation of diffusion), x_0 (energy transfer distance), and p (surface recombination probability).

enced by band offset as well as surface coverage, a variation within one or two orders of magnitude is reasonable in this case.

4.2 Time-resolved Photoluminescence

In a second experiment, we measured the time-resolved photoluminescence of Alq_3 on SnO_2. Integrating the emission spectrum from $\lambda = 500$ to 560 nm, we obtain the intensity profile as a function of time. Using a single exponential decay, we extract the exciton lifetime of each sample and plot it against Alq_3 thickness in Figure 4-4. To understand the time evolution of exciton dynamics, we employ the Monte Carlo model to simulate the intensity profile as a function of time. Fixing $\tau_\infty = 17.4$ nsec [45], we optimize the input parameters through trial and error. We find that when the exciton diffusion length is set at ~80 Å, the exciton lifetime predicted by the simulation matches reasonably well with the experimental results, and the quenching mechanism can be perfect surface quenching, energy transfer with $x_0 \simeq 10$–25 Å, or both. Different time step sizes have also been used, and there is no

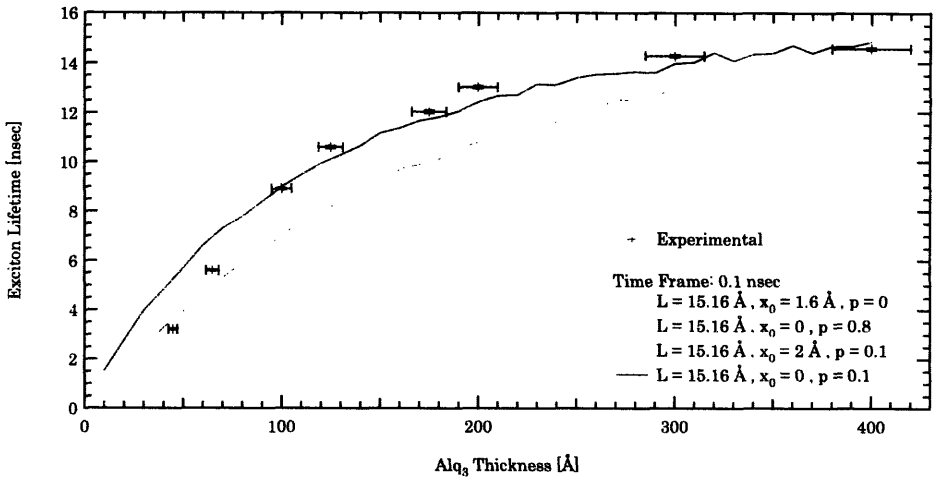

Figure 4-5: Comparison between experimental and simulation results: Exciton lifetime is plotted against Alq_3 film thickness. In this case, the exciton diffusion length is fixed at 200 Å. Input parameters are denoted by L (standard deviation of diffusion), x_0 (energy transfer distance), and p (surface quenching probability).

noticeable change in the results. On the other hand, if we fix the exciton diffusion length at 200 Å and the energy transfer distance at ~1.5 Å, as derived from the steady state analysis, we find that the simulation does not agree with the experimental results (Figure 4-5), especially for thinner Alq_3 layers.

Consequently, there appears to be an alarming discrepancy between the steady state analysis and the time-resolved photoluminescence simulation. In the next section, we will present a solution to reconcile these two models.

4.3 Optical Interference and Alq_3 Absorption

Although the emission of Alq_3 does not seem to be affected by microcavity or optical interference effects, it is not necessarily the case with the excitation source. Using the T-matrix model derived in Appendix B, we find that Alq_3 absorption at $\lambda = 408$ nm fluctuates with film thickness, as shown in Figure 4-6. This oscillation is caused by the optical interference from the reflections at the Alq_3/air, Alq_3/SnO_2, and SnO_2/glass interfaces. With this in mind, we plot the corrected photoluminescence efficiency of Alq_3 in Figure 4-7. By fixing the exciton diffusion length at 80 Å, we obtain a

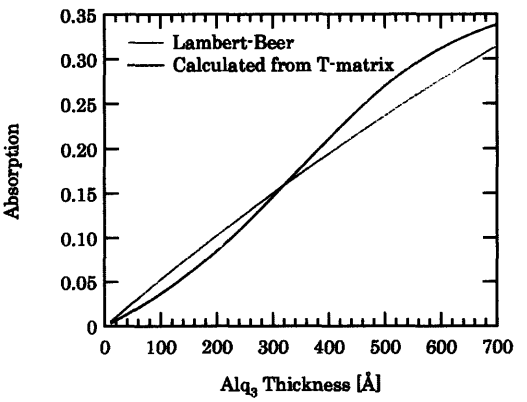

Figure 4-6: Alq_3 absorption calculated from the Beer-Lambert Law and from T-matrices.

reasonably good fit for the case of a perfect quenching surface with no energy transfer, and the fitting error is 146.2. As we apply energy transfer to the analytical model, we find that with increasing energy transfer distance, the fitting error reduces: 140.9 for $x_0 = 10$ Å, 118.2 for 25 Å, and 103.5 for 40 Å. In addition, as we fix energy transfer at the aforementioned distances, the fitting quality is not affected by whether the surface quenching velocity is finite or infinite. This indicates that with a lower mobility and a longer energy transfer distance, there is a higher chance for excitons to energy transfer to the absorbing layer before they reach the interface. Thus, the population density at the quenching interface is effectively zero, regardless of the surface quenching velocity. In all, after optical correction, we have reconciled the analytical model with the Monte Carlo simulation.

4.4 Surface Modifications

To separate surface quenching from energy transfer, we have explored two methods to reduce the quenching effect due to one mechanism relative to the other. In one approach, we attempted to eliminate surface effects by depositing a 20 Å thick BCP layer on SnO_2. This approach, however, is ineffective, as we observed that BCP poorly wets SnO_2 surfaces. In the other approach, we applied a self-assembled monolayer

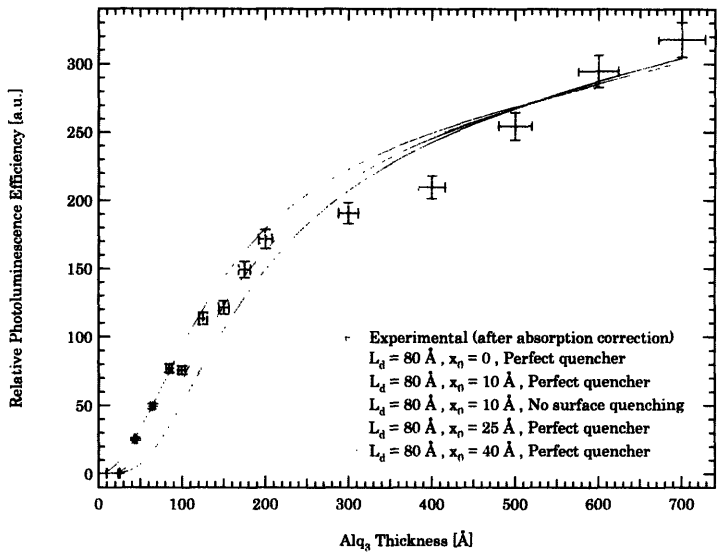

Figure 4-7: Corrected photoluminescence efficiency and various fitting models. Input parameters are denoted by L_d (exciton diffusion length) and x_0 (energy transfer distance).

of silanated molecules to SnO_2. We found that with the self-assembled monolayer technique, an ultra-thin, uniform, and nonquenching coating can be achieved.

It has been reported that a thin layer (~20 Å) of a wide bandgap organic material such as bathocuproine (BCP) can prevent exciton dissociation at a quenching interface [60]. Thus, we explored this approach by depositing BCP[2] of various thickness on SnO_2. As-deposited films were examined under AFM, and it was observed that instead of covering the surface uniformly, BCP segregated into small islands as illustrated in Figure 4-8. Furthermore, even with an 80 Å thick film, the surface coverage was only about 70–80%. Consequently, a thin and uniform nonquenching layer cannot be attained with BCP.

In another experiment, we explored the self-assembled monolayer (SAM) technique. We used 3-aminopropyltriethoxysilane (APTES)[3] as a precursor, which covalently binds to oxide surfaces through a process shown in Figure 4-9. To ensure repeatability, we applied the following procedure:

[2]BCP was provided by H.W. Sands Corp. The deposition conditions were the same as those used for Alq_3 (Chapter 2).

[3]Manufactured by Pierce Biotechnology, Inc.

Figure 4-8: AFM scans of a SnO_2 thin film after 20 Å thick BCP deposition: (a) height and (b) phase.

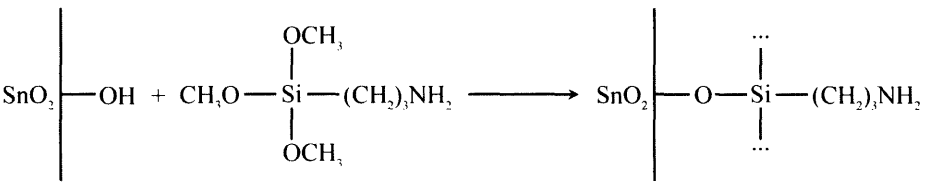

Figure 4-9: APTES reacts with the hydroxyl groups (–OH) on oxide surfaces to form a uniform monolayer.

1. Mix 2% APTES with 93% ethanol and 5% deionized water by volume. Adjust the pH with acetic acid to 4.5–5.5.

2. Immerse clean oxide substrates in the mixture for one and a half minutes.

3. Rinse substrates in ethanol. Blow dry with nitrogen.

4. Heat substrates at 100°C for ten minutes.

Through contact angle measurements, we found that the surface had been modified by the aforementioned recipe, as the contact angle increased from ~0° to ~45°. The uniformity of SAM was verified through AFM, which shows that there was no significant change in the surface roughness (~6 Å) before and after the treatment. Finally, with ellipsometry, we found that the monolayer thickness was about 6.5 ± 3.0 Å.

L_d [Å]	x_0 [Å]	d_{SAM} [Å]	Alq_3/SnO_2	$Alq_3/SAM/SnO_2$
80	10	6.5	0.17	0.46
80	25	6.5	0.13	0.21
75	25	6.5	0.14	0.22
70	25	6.5	0.16	0.22
65	30	6	0.15	0.19
70	25	4.5	0.16	0.19
72	23	4	0.16	0.19
75	20	3	0.16	0.19

Table 4.2: Predicted emission intensities of 100 Å Alq_3/300 Å SnO_2/glass and 100 Å Alq_3/SAM/300 Å SnO_2/glass relative to 100 Å Alq_3/glass. Input parameters are denoted by L_d (exciton diffusion length), x_0 (energy transfer distance), and d_{SAM} (SAM thickness). Exciton generation rate is assumed to be uniform.

To show that there is negligible or no surface quenching at the SAM/Alq_3 interface, we deposited 100 Å thick Alq_3 on bare glass substrates and glass substrates treated with SAM. Through photoluminescence measurement, we found that the variation in the peak emission intensity was within 5%, which indicates that SAM surfaces are as inert as those of clear glass substrates. In another experiment, we deposited 100 Å thick Alq_3 on (1) bare glass, (2) 300 Å SnO_2/glass, and (3) SAM/300 Å SnO_2/glass substrates. Based on T-matrices, Alq_3 absorption in sample 1 is expected to be 0.048, and in samples 2 and 3, the absorption is expected to be 0.026. In other words, if there is no energy transfer between Alq_3 and SnO_2, then the emission intensity from sample 3 should be about 0.54 relative to sample 1. The actual relative intensity was found to be 0.19, indicating that there must be energy transfer from Alq_3 to SnO_2.

Assuming that SAM acts like a uniform spacer, we modified the analytical model to analyze the experimental results. Through trial and error, we find that the exciton diffusion length is likely in the range of 70–75 Å, the energy transfer distance 20–25 A, and the SAM thickness 3–4.5 Å (Table 4.2). Although both the exciton diffusion length and the energy transfer distance agree with earlier results, we note that the monolayer thickness in the range of 3–4.5 Å is probably an underestimate compared to the measured value of 6.5 ± 3 Å. This can be attributed to the uncertainty in Alq_3 absorption and other experimental errors.

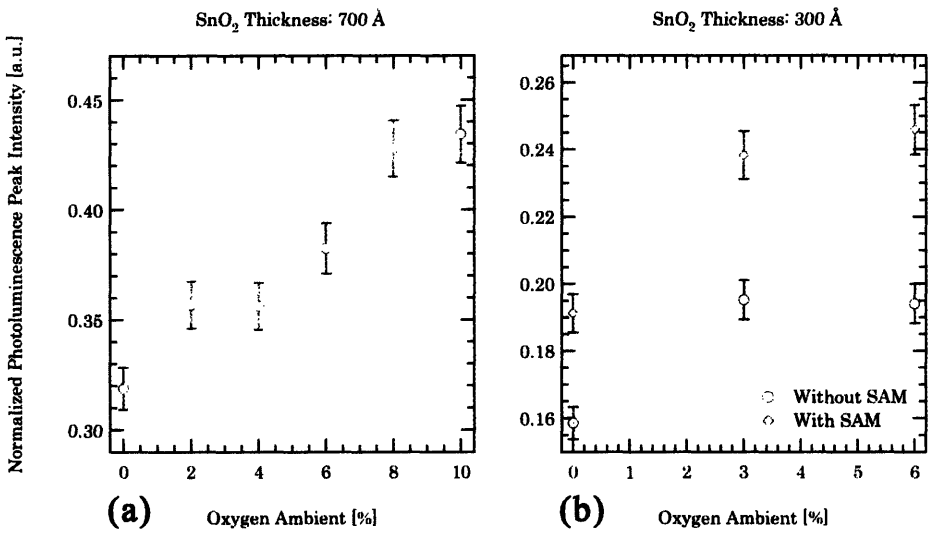

Figure 4-10: Photoluminescence of 100 Å thick Alq_3 thin film on SnO_2 substrates grown with different oxygen content in the plasma-forming gas mixture: (a) 700 Å thick SnO_2 films and (b) 300 Å thick SnO_2 films with and without application of self-assembled monolayer.

4.5 Excess Oxygen and the Effects on Photoluminescence Quenching

As shown in Appendix A, the electrical and optical properties of SnO_2 can be modified by introducing excess oxygen into the sputtering gas mixture. It is therefore of interest to investigate how excess oxygen affects photoluminescence quenching by SnO_2. In the following experiment, we evaporated 100 Å thick Alq_3 onto 700 Å thick SnO_2 films that were deposited under different oxygen contents (0–10%) in the sputtering ambient. We measured the time-integrated photoluminescence of these samples and that of Alq_3 just on glass, which is used for normalization. Experimental results are shown in Figure 4-10a, which shows that the peak emission intensity of Alq_3 on SnO_2 increases with the amount of oxygen in the sputtering ambient.

To explain the apparent increase in the Alq_3 emission intensity, we consider the following possibilities: (1) increase in Alq_3 absorption, (2) increase in the reflectance at the Alq_3/SnO_2 interface, and (3) reduction in photoluminescence quenching. We employ T-matrices to assess the first two cases. Assuming that there is no signifi-

cant change in the real refractive index of SnO_2 and only the extinction coefficient is reduced by excess oxygen,[4] then the absorption of Alq_3 is found to be ~0.042 for all samples, regardless of the oxygen content. Under the same assumptions, we find that the change in reflectance at the Alq_3/SnO_2 interface at $\lambda = 530$ nm is also small: 0.081 for 0% O_2, 0.084 for 2%, 0.085 for 4%, and 0.086 for 6–10%. Consequently, it is probably the case that excess oxygen in the sputtering ambient reduces photoluminescence quenching by SnO_2.

Applying the analytical model, we note that given a perfect quencher with no energy transfer, the expected normalized emission intensity is 0.337. Since the emission intensity exceeds 0.35 with with oxygen content greater than 2%, these SnO_2 surfaces can no longer be modeled by the perfect quencher case, which also implies that the energy transfer distance has been drastically reduced so that it is small relative to the exciton diffusion length. As an estimate, assuming the exciton diffusion length at 70 Å and no surface quenching, we find that the energy transfer distance decreases from ~10 Å for 0% O_2, to ~2 Å for 2–4% O_2, and finally to ~1.2 Å for 8–10% O_2. Because of the uncertainty in the Alq_3 absorption, the energy transfer distance extracted from this experiment is lower than previous results.

In another experiment, we applied SAM to 300 Å thick SnO_2 films deposited with various oxygen contents (0, 3, and 6%) and evaporated 100 Å thick Alq_3 onto these substrates. Normalized peak emission intensity of each sample—both with and without SAM—is plotted in Figure 4-10b, which shows that the photoluminescence intensity is always greater with the monolayer, regardless of the oxygen content. To model this new structure, we used ellipsometry to measure the refractive index of SAM, which is found to be about 1.35 at $\lambda = 633$ nm. Assuming that $n_{SAM} = 1.35$ is constant for the entire visible spectrum, we find that neither the Alq_3 absorption nor the reflectance at the Alq_3/SnO_2 interfacedue is affected by the introduction of SAM. Thus, results from this experiment show that even with a ~6 Å spacing layer, photoluminescence quenching is reduced with increasing oxygen content in the sputtering gas mixture, indicating that energy transfer must be the dominant quenching

[4]This is discussed in more detail in Appendix A.

mechanism for pure SnO_2 films.

Based on the results from previous experiments, we speculate that changes in the optical properties of SnO_2 due to excess oxygen cause the reduction in photoluminescence quenching. By removing oxygen vacancies in pure SnO_2, excess oxygen reduces the density of free carriers and defect electronic states, which are responsible for the absorption in the visible spectrum. As a result, the extinction coefficient of SnO_2 is reduced by excess oxygen, and so is the spectral overlap between the emission of Alq_3 and the absorption of SnO_2, thereby shortening the energy transfer distance from Alq_3 to SnO_2.

4.6 Summary

Experimental results indicate that photoluminescence quenching takes place near the Alq_3/SnO_2 interface. We have applied both the analytical model and the Monte Carlo simulation to analyze the emission of Alq_3. After optical correction, we have found that both models agree with each other when the exciton diffusion length in bulk Alq_3 is in the range of 70–80 Å and the main quenching mechanism is energy transfer with a distance in the range of 10–30 Å. We have also shown that the energy transfer distance is reduced by excess oxygen in the sputtering gas mixture, from which we speculate that excess oxygen causes a reduction in the spectral overlap between the emission of Alq_3 and the absorption of SnO_2 by lowering the extinction coefficient of the as-deposited SnO_2 films.

Chapter 5

Final Remarks

IN an attempt to understand how excitons in organic solids behave in the presence of a transparent conducting oxide, we have conducted a basic study on photoluminescence quenching of Alq_3 on sputtered SnO_2 substrates. In Chapter 2, we described the experimental setup and other measurement techniques used for this work. In Chapter 3, we presented a physical model for exciton dynamics in amorphous organic solids. In Chapter 4, we demonstrated that exciton dynamics can be modeled and characterized with just a few parameters using both the analytical model and the Monte Carlo simulation. The exciton diffusion length in bulk Alq_3 extracted from these results is found to be in the range of 70–80 Å, and resonant energy transfer from Alq_3 to SnO_2 appears to be the dominant quenching mechanism. By introducing excess oxygen in the sputtering gas mixture during SnO_2 deposition, we showed that the energy transfer distance decreases from 10–25 Å for 0% O_2 to less than 2 Å for 10% O_2. Based on the experimental results, we speculate that as excess oxygen removes oxygen vacancies in sputtered SnO_2, the as-deposited film contains less defect states and becomes more transparent to Alq_3 emission. As the spectral overlap between the emission of Alq_3 and the absorption of SnO_2 is reduced by excess oxygen, the energy transfer distance is shortened. Consequently, the photoluminescence yield of Alq_3 on SnO_2 increases with the amount of O_2 in the sputtering ambient during the deposition of SnO_2.

In the wake of a severe time constraint, many ideas have been considered but not

fully developed. Thus, we will hereby make a few suggestions for future research:

- **In situ photoluminescence measurement**. Time-integrated photoluminescence measurements can be vastly simplified if measurements are made while the organic material is being evaporated onto the substrate. One of the main benefits is that measurements now take place in vacuum, thereby eliminating the possibility of photoluminescence quenching at the otherwise organic/air interface. In addition, if the growth rate is constant, then an automated system can be devised to take measurements at evenly spaced time periods, which also ensures evenly spaced sample thickness.

- **Improved optical model**. Presently, our optical model based on T-matrices allows us to calculate only the overall absorption of a whole layer. An improved optical model that can trace the absorption at any location will allow us to analyze and to model the photoluminescence of Alq_3 to a greater accuracy.

- **Characterizing SnO_2 surface states**. Although AFM and XRD can reveal the surface morphology and crystallinity of sputtered SnO_2 films, these techniques cannot reveal much about the Sn/O ratio, surface defects, or the density of oxygen vacancies and bandgap states. A more comprehensive characterization can be accomplished with ultraviolet photoelectron spectroscopy, and ion scattering spectroscopy can also be used to probe the composition and structure of SnO_2 films.

- **Doping with different elements**. The electrical and optical properties of SnO_2 can be modified not only by excess oxygen but also by other elements such as fluorine and antimony. It will be interesting to compare the effects on photoluminescence quenching due to different doping elements.

In all, we have presented a model for analyzing photoluminescence quenching of an organic thin film due to a transparent conductive oxide. Although much has yet to be done, we hope that this work can be used as a guide for future research and development.

Appendix A

Characterizing Sputtered SnO_2 Thin Films

IN this section, we will study how excess oxygen in the sputtering ambient influences the structural, electrical, and optical properties of sputtered SnO_2 films. We will show that as-deposited SnO_2 films are either amorphous or nanocrystalline, and their crystallinity does not improve with increasing oxygen content in the sputtering ambient. Next, we will present experimental results and discuss how as-deposited SnO_2 films become more resistive and transparent with excess oxygen in the sputtering gas mixture.

A.1 Structural Properties

We characterized the structural properties of as-deposited SnO_2 thin films with X-ray diffraction (XRD). Figure A-1a shows that as-deposited SnO_2 (0% O_2) films do not contain sufficiently large grain sizes to yield diffraction patterns and the crystallinity does not improve with film thickness from 700 to 1,300 Å. Figure A-1b shows that there also seems to be no effect on the crystallinity even with an increasing amount of oxygen in the plasma-forming gas mixture. Although there appears to be a peak at $2\Theta \simeq 29°$ with the 11 and 40% O_2 samples, it does not match with any known SnO_2 crystallographic plane or any other element that could have possibly been present

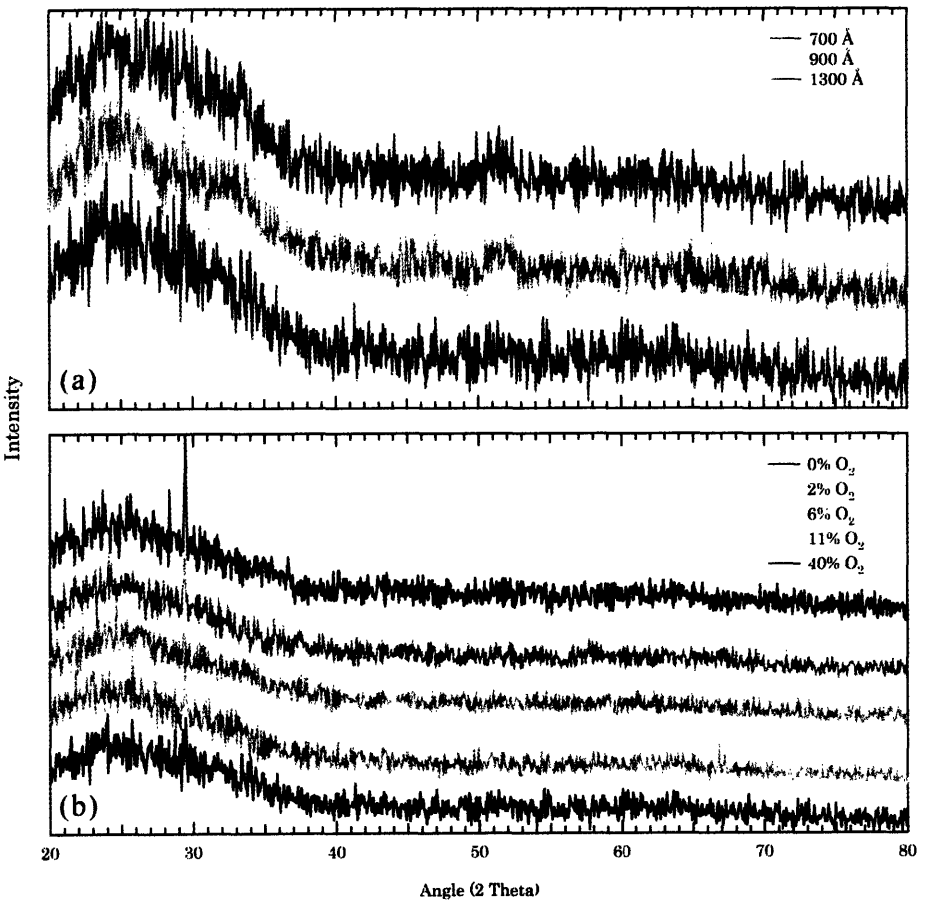

Figure A-1: X-ray diffraction spectra of as-deposited SnO_2 thin films on glass substrates: (a) SnO_2 (0% O_2) with different thickness and (b) SnO_2 deposited with different amounts of oxygen in the sputtering gas mixture. These films are either amorphous or nanocrystalline because they do not appear to contain sufficiently large grain sizes to yield diffraction patterns.

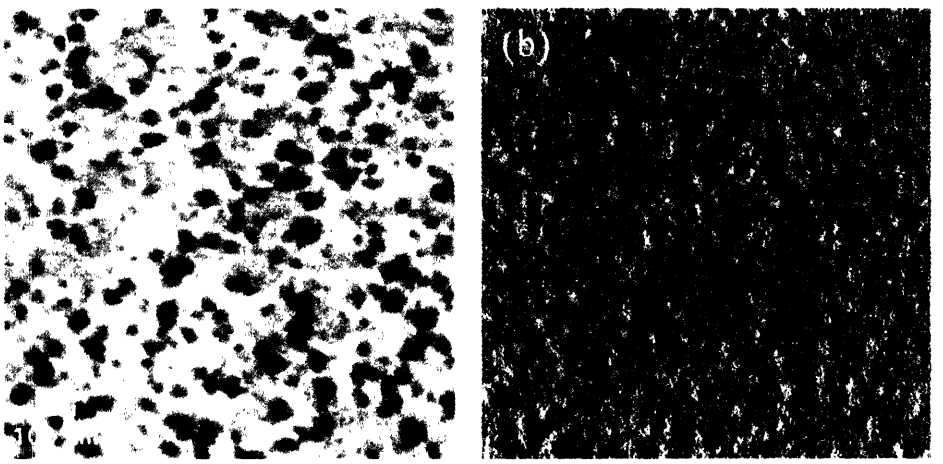

Figure A-2: AFM scans of an as-deposited 700 Å thick SnO_2 film (0% O_2): (a) height and (b) phase. The root-mean-square roughness of this sample is about 5 Å.

in the sputtering chamber. These XRD studies reveal that as-deposited SnO_2 films are either amorphous or nanocrystalline. Our observations are consistent with those reported in literature [21, 61].

Surface morphology was characterized with AFM. Under the deposition conditions detailed in Chapter 2, the surfaces of SnO_2 films appear uniform and smooth (Figure A-2). Excess oxygen in the sputtering gas does not seem to affect the surface roughness, which varies between 3.5 and 6.5 Å for 700 Å thick SnO_2 films deposited with different oxygen contents (0, 11, and 40%).

A.2 Electrical Properties

It is generally believed that the prevailing donor defect in pure SnO_2 arises from oxygen vacancies [22]. Since Equation 2.1 suggests that the density of free electrons is inversely related to the partial pressure of oxygen, introducing oxygen to the sputtering gas mixture should have a major effect on the electrical properties of the resulted films. Using the van der Pauw method [34], we have observed that the sheet resistance increases with oxygen content (Figure A-3a) and that the carrier density is reduced by about one order of magnitude for every 4% of excess oxygen in the plasma-forming

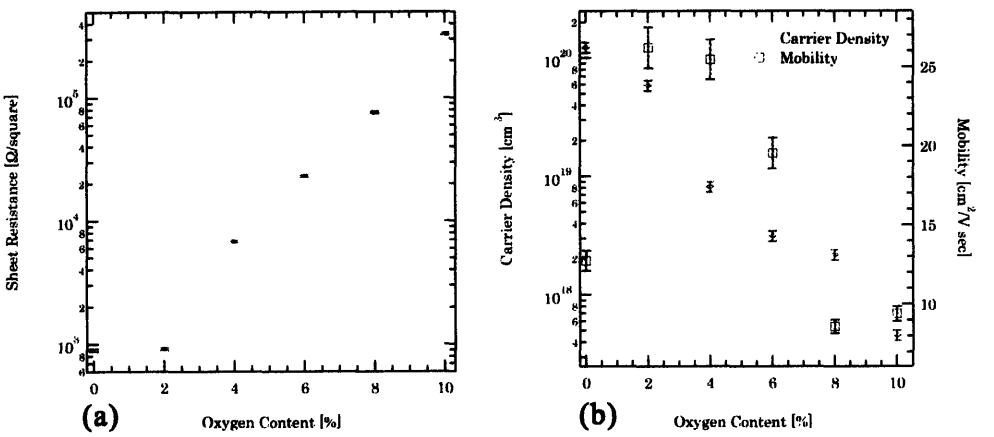

Figure A-3: Excess oxygen and the effects on the electrical properties of sputtered SnO_2 thin films: (a) Sheet resistivity of SnO_2 films (700 Å) is plotted against the percentage of O_2 flow in the sputtering gas mixture; (b) carrier density and Hall mobility are plotted against the percentage of O_2 flow in the sputtering gas mixture. The total Ar/O_2 gas flow was fixed at 10 sccm, and the total gas pressure was set at 3 mTorr.

gas mixture (Figure A-3b). Experimental results also show that as the oxygen content increases from 0 to 2%, the Hall mobility first rises from 12.7 to 26.2 cm^2/V sec, but beyond 2%, it decreases with additional oxygen in the sputtering gas mixture (Figure A-3b). The initial increase in the mobility is likely due to reduced ionized impurity scattering, which has been observed in other metal oxides (e.g. ITO) deposited with various oxygen partial pressures [62, 63]. When the carrier density is greater than 10^{21} cm^{-3}, the effect of ionized impurity scattering scales approximately with n^{-w}, where n is the carrier density and w is typically $\sim 2/3$ [63].† Consequently, when the oxygen content is between 0 and 2%, excess oxygen has opposite effects on the carrier density and mobility, and the sheet resistance appears unchanged between these two points (Figure A-3a). As the carrier density drops below 10^{20} cm^{-3} with oxygen content greater than 2%, ionized impurity scattering is no longer the dominant scattering mechanism. Above this point, excess oxygen in the SnO_2 films not only distorts the lattices but also creates potential traps, which capture free electrons

†Because of a relatively small sample size, we are unable to confirm the value of w in this experiment.

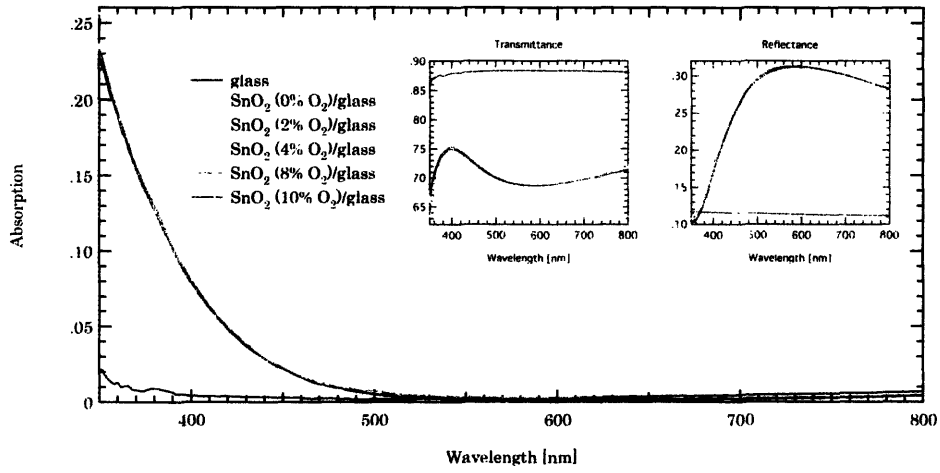

Figure A-4: Absolute absorption of 700 Å SnO_2/glass samples with the transmittance and reflectance spectra shown in the inset.

to form negatively charged scattering sites [63]. Therefore, when the oxygen content is greater than 2%, excess oxygen has negative effects on both the carrier density and mobility, and the sheet resistance increases exponentially with oxygen content.

A.3 Optical Properties

Since the optical properties of a material are closely related to its electrical properties, excess oxygen in the sputtering environment should also have a major impact on the optical properties of the as-deposited films. The transmittance and reflectance spectra of different SnO_2/glass samples were measured, from which the absolute absorption[†] of each sample was obtained (Figure A-4). Experimental results show that the SnO_2/glass structure as a whole becomes less absorptive with increasing oxygen content. To explain this variation in absorption, three possible causes have been identified: (1) changes in optical scattering, (2) changes in film thickness, and (3) changes in the index of refraction.

Based on the structural analysis presented previously, we contend that there is little change in optical scattering. Because the input power, ambient pressure, and

[†]By the conservation of energy, the absolute absorption is given by $A = 1 - T - R$, where T is the transmittance and R the reflectance.

growth rate were kept constant for each sample during the deposition process, the density of the as-deposited film should be uniform, thereby eliminating Brillouin scattering. Since as-deposited SnO_2 films are either amorphous or nanocrystalline and the crystallinity does not improve with excess oxygen, random inhomogeneities of the refractive index, which are responsible for Rayleigh scattering, should not be affected with excess oxygen, either, thereby eliminating any change in Rayleigh scattering. Furthermore, given a thickness of 700 Å, it is unlikely for a film so thin to contain sizable air pockets, which can cause Mie scattering, while still retaining a smooth surface. Therefore, by structural considerations, we conclude that variation in the overall absorption is not caused by changes in optical scattering.

Although we can dismiss optical scattering by physical reasoning alone, variation in film thickness must be verified through direct observation. In general, the uncertainty in thickness arises from experimental errors occurred during the deposition process. For example, since the sputtering system requires manual operations for each deposition process, if the growth rate is about 1–2 Å/sec, then there probably will be an error of about 1–2 Å in the actual thickness of the sample with respect to the number registered by the thickness monitor. Moreover, to calculate film thickness, the thickness monitor requires a number of parameters, one of which is the density of the sputtered film. Although the density of pure SnO_2 is 6.9 g/cm^3, which was used for all depositions, it may vary with additional oxygen incorporated into the sputtered film. Nevertheless, we confirmed through ellipsometry that under the same assumed density, the variation in thickness does not exceed 3 Å among 300 Å thick SnO_2 films deposited with 0, 3, and 6% O_2 in the sputtering gas. Thus, we conclude that variation in the overall absorption is not caused by changes in film thickness or density.

Eliminating optical scattering and thickness variation, we deduce that the index of refraction must have been modified by excess oxygen. Since SnO_2 is a weakly absorptive material in the visible spectrum, to accurately resolve the complex index of refraction, sample thickness must be precisely determined, which, unfortunately, is not available for the 700 Å SnO_2 films. Nevertheless, we argue that most of the change

takes place in the extinction coefficient only. Through ellipsometry, we found that at 633 nm the real index of refraction is not affected by excess oxygen: 1.994 ± 0.010 for 0% O_2, 1.996 ± 0.010 for 3% O_2, and 2.014 ± 0.010 6% O_2. On the other hand, at this wavelength, the overall absorption is reduced by about a factor of two with the first 2% O_2, and it is further reduced by another factor of five with 4–10% O_2. Given that the free electrons in SnO_2 are reponsible for the optical absorption near the infrared range, and that the electronic transition from the valence band to the empty bandgap states is reponsible for the optical absorption in the visible and near ultraviolet range, since excess oxygen removes the intrinsic donors in pure SnO_2 and reduces its carrier density, it follows that the extinction coefficient should also decrease with increasing oxygen content. As a result, the SnO_2 films should become less absorptive with increasing oxygen content, which is consistent with the experimental results.

A.4 Summary

In this section, we have shown that as-deposited SnO_2 thin films are amorphous or nanocrystalline, and the crystallinity does not improve with film thickness from 700 to 1,300 Å or excess oxygen (up to 40%) in the sputtering gas mixture. The surface of as-deposited SnO_2 appears uniform and smooth. Introducing oxygen in the deposition process has a major effect on the conductivity of the as-deposited films, as the carrier density is reduced by about one order of magnitude for every 4% O_2 in the sputtering ambient. Finally, with increasing oxygen content, the SnO_2/glass samples become less absorptive, from which we deduce that because excess oxygen reduces the density of bandgap states as well as that of free electrons, the extinction coefficient decreases with increasing oxygen content, thereby lowering the overall absorption.

THIS PAGE INTENTIONALLY LEFT BLANK

Appendix B

Optical Model Based on T-matrices

GIVEN a multilayer structure, optical interference and microcavity effects may arise if there is a significant index mismatch. In this section, we will describe an optical model based on T-matrices and show that it can be used to produce a reasonable normalization factor for photoluminescence measurements.

B.1 T-matrix Derivation

The following implementation was originally developed by M. Scott Bradley [64].† We assume that incident wave is traverse-electric (TE) polarized. Thus, the **E** field must be continuous across any boundary. Next, we consider the following three-layer structure:

$$\begin{array}{ccccc} 1 & & 2 & & 3 \\ \tilde{n}_1 & \Big| _a & \tilde{n}_2 & \Big| _b & \tilde{n}_3 \end{array}$$

where $\tilde{n}_{1,2,3}$ denotes the complex refractive index of layer 1, 2, or 3; the interface between layers 1 and 2 is denoted by a and that between layers 2 and 3 by b. Furthermore, if we denote the forward-traveling direction by '+' and the backward-traveling

†For a detailed review on electromagnetic waves in macroscopic media, readers are referred to Reference 40.

direction by '$-$', then the $\mathbf{E}$ field of the transmitted wave $t_{12}\mathbf{E}_{1a}^{+}$ from layer 1 across a, where t_{12} is the transmission coefficient from layer 1 to 2, must be equal to the sum of the forward-traveling wave in layer 2 and the reflected backward-traveling wave at a, i.e. $\mathbf{E}_{2a}^{+} + r_{2a}\mathbf{E}_{2a}^{-}$, where r_{2a} is the reflection coefficient at a in layer 2, and vice versa. Therefore, the boundary matching condition at a is

$$\begin{bmatrix} \mathbf{E}_{1a}^{+} \\ \mathbf{E}_{1a}^{-} \end{bmatrix} = \frac{1}{t_{12}} \begin{bmatrix} 1 & r_{2a} \\ r_{2a} & 1 \end{bmatrix} \begin{bmatrix} \mathbf{E}_{2a}^{+} \\ \mathbf{E}_{2a}^{-} \end{bmatrix} \tag{B.1}$$

In particular, r_{2a} and t_{12} are given by:

$$r_{2a} = \frac{\tilde{n}_2 - \tilde{n}_1}{\tilde{n}_2 + \tilde{n}_1} \quad , \quad t_{12} = \frac{2\tilde{n}_1}{\tilde{n}_2 + \tilde{n}_1} \tag{B.2}$$

Next, if we define $\beta_2 = 2\pi\tilde{n}_2 d_2/\lambda$, where d_2 is the thickness of layer 2 and λ the wavelength of interest, then the propagated wave from interface a to b in layer 2 is

$$\begin{bmatrix} \mathbf{E}_{2a}^{+} \\ \mathbf{E}_{2a}^{-} \end{bmatrix} = \begin{bmatrix} e^{-\imath\beta_2} & 0 \\ 0 & e^{\imath\beta_2} \end{bmatrix} \begin{bmatrix} \mathbf{E}_{2b}^{+} \\ \mathbf{E}_{2b}^{-} \end{bmatrix} \tag{B.3}$$

If we denote the boundary matching matrix at interface a by V_{12}, the propagation matrix from a to b by V_2, and the boundary matching matrix at b by V_{23}, then the we obtain the following for the overall three-layer structure:

$$\begin{bmatrix} \mathbf{E}_{1a}^{+} \\ \mathbf{E}_{1a}^{-} \end{bmatrix} = V_{12}V_2V_{23} \begin{bmatrix} \mathbf{E}_{3b}^{+} \\ \mathbf{E}_{3b}^{-} \end{bmatrix} \tag{B.4}$$

In particular, since layer 3 is the last layer, $\mathbf{E}_{3b}^{-} = 0$. Furthermore, if we define the overall reflection coefficient $r = \mathbf{E}_{1a}^{-}/\mathbf{E}_{1a}^{+}$ and the transmission coefficient $t = \mathbf{E}_{3b}^{+}/\mathbf{E}_{1a}^{+}$, then Equation B.4 can be rewritten as

$$\begin{bmatrix} 1 \\ r \end{bmatrix} = V_{12}V_2V_{23} \begin{bmatrix} t \\ 0 \end{bmatrix} \tag{B.5}$$

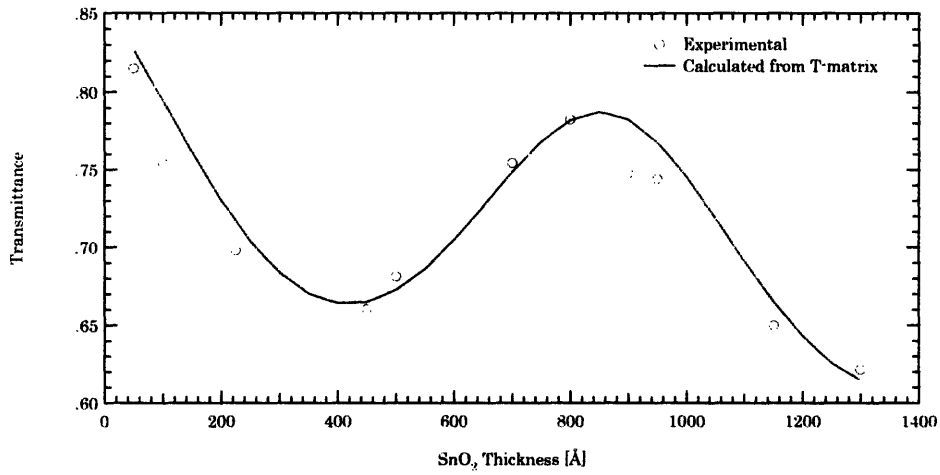

Figure B-1: Experimental and theoretical transmittance of 100 Å $Alq_3/SnO_2/1$ mm glass samples at 408 nm is plotted against the thickness of SnO_2.

And if $\tilde{n}_1 = \tilde{n}_3$ (e.g. air), then the reflectance and transmittance of the whole structure are given by $R = |r|^2$ and $T = |t|^2$, respectively. By the conservation of energy, the absorption is $A = 1 - T - R$.

To obtain the absorption of any particular layer, we calculate the Poynting vector $\mathbf{S}$ at each of the two interfaces $1a$ and $3b$:

$$\mathbf{S}_{1a} = (\mathbf{E}^+_{1a} + \mathbf{E}^-_{1a}) \times (\mathbf{H}^+_{1a} - \mathbf{H}^-_{1a}) \tag{B.6}$$

$$\mathbf{S}_{3b} = (\mathbf{E}^+_{3b} + \mathbf{E}^-_{3b}) \times (\mathbf{H}^+_{3b} - \mathbf{H}^-_{3b}) \tag{B.7}$$

where $\mathbf{H} = \sqrt{\mu_0/\epsilon_0}\tilde{n}\mathbf{E}$. Therefore, the amount of incident power absorbed by any particular layer i is

$$A_i = \left| \frac{\langle \mathbf{S}_{1a} \rangle - \langle \mathbf{S}_{3b} \rangle}{\langle \mathbf{S}_0 \rangle} \right| \tag{B.8}$$

where $\langle \mathbf{S} \rangle = \Re\{\mathbf{S}\}/2$ and $\langle \mathbf{S}_0 \rangle$ is the initial input power.

B.2 Comparison with Experimental Results

To test the predictions made by T-matrices, we measured the transmittance of 100 Å $Alq_3/SnO_2/1$ mm glass samples with various SnO_2 thickness. Theoretical transmit-

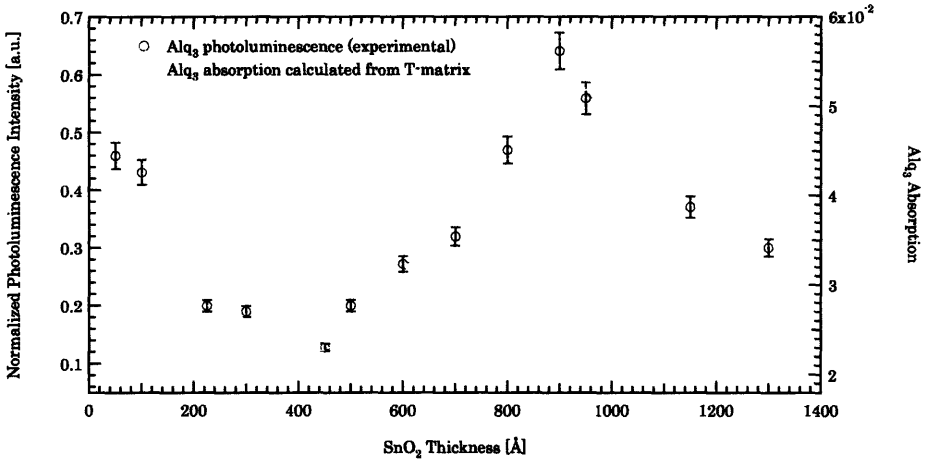

Figure B-2: Photoluminescence of 100 Å Alq_3/SnO_2/glass samples with various SnO_2 thickness. Superimposed on this figure is the absorption of the Alq_3 layer predicted by T-matrices at $\lambda = 408$ nm.

tance was calculated by assuming the refractive indices of Alq_3, SnO_2, and borosilicate (BK7) glass as those published in literature [45,54]. To approximate the diffusive nature of a thick ($\sim$1 mm) glass substrate, we vary the glass thickness by a full cycle of $(2\pi/\lambda)^{-1}$ and average over the resulting theoretical transmittance. A comparison between the theoretical and the experimental transmittance at 408 nm[†] is shown in Figure B-1, which shows that the predictions made by T-matrices are in good agreement with the experimental results.

In another experiment, we measured the photoluminescence of 100 Å Alq_3/SnO_2/ glass samples with various SnO_2 thickness and normalized their emission with respect to that of 100 Å Alq_3/glass. Given the same deposition conditions, these samples should not exhibit different photoluminescence yield, but experimental results show that the emission intensity of Alq_3 oscillates with SnO_2 thickness (Figure B-2). This can be explained, in part, by the optical interference with the excitation source in the Alq_3 layer because the Alq_3 absorption predicted by T-matrices oscillates in phase with the corresponding photoluminescence. Nonetheless, the peak-to-peak ratio predicted by T-matrices is still smaller than that from the experimental results by as

[†]This particular wavelength was chosen because a 408 nm laser source was used for all steady state photoluminescence measurements (Chapter 2).

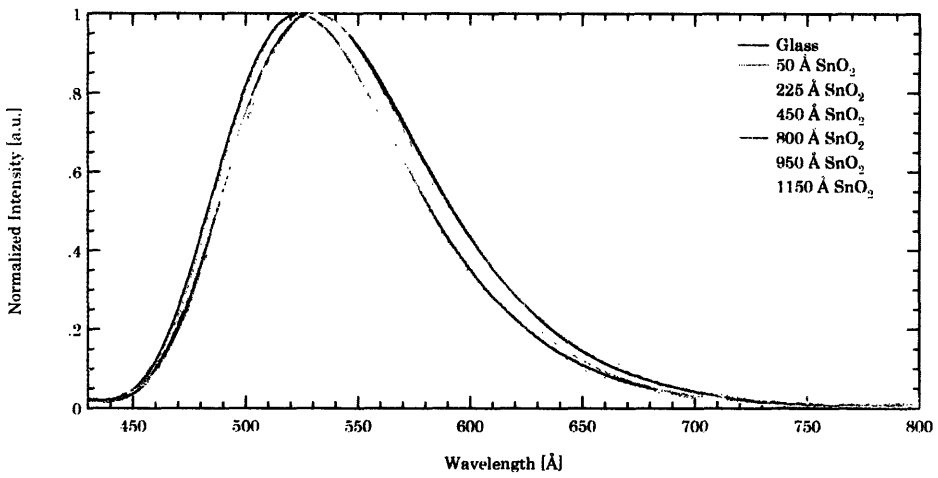

Figure B-3: Normalized photoluminescence spectra of 100 Å Alq_3/SnO_2/glass samples of various SnO_2 thickness. The emission peaks of the 800 and 950 Å samples are blue-shifted by about 7 nm with respect to other samples, indicating a weak microcavity effect on the photoluminescence of Alq_3.

much as a factor of two. Thus, we speculate that there are additional optical effects. Comparing the normalized photoluminescence spectra of these samples (Figure B-3), we note that the 800 and 950 Å samples are blue-shifted by about 7 nm. As a result, there appears to be some microcavity effect on the emission. On the other hand, because the spectral shift is relatively small, this microcavity effect is probably too weak to induce a large variation in the photoluminescence yield. Therefore, it is likely the case that the glass substrate does not completely dephase the incident wave. Since the excitation source is coherent, the actual optical effects should appear to be much stronger than those of incoherent light, which is assumed for the T-matrix calculations.

B.3 Matlab Script for T-matrices

```
% M. Scott Bradley, Jun Mei
% T-matrix simulation of Alq3 on SnO2 on glass

% wavelength=[351:1:799]*10^-9;
```

```
% wavelength=530*10^-9;
%
% % at 530 nm (~2.3 eV), tin oxide k is ~0, n is ~2.04
% % alq3's is: n=1.75, k=0
% nalq3=1.75;
% nsno2=2+j*0.025;
%
% % dmeas=[50 100 225 450 500 700 800 900 950 1150 1300]*10^-10; % m
% % Tmeas=[89.39 86.235 80.759 73.021 73.137 74.326 78.309
% 83.187 83.692 87.064 82.924]/100;
%
% % at 700 A:
% Tmeas=[74.326 76.231 76.609 76.75 76.82 77.031];
% pcts=[0 2 4 6 8 10];
%
% %% from changing k by hand
% sno2n=[2];
% sno2k=[0.025 0.008 0.004 0.003 0.002 0.0001];

% at 408 nm (3.045 eV), tin oxide k is ~0.033, n is ~2.145
% alq3's is: n=1.85, k=0.15

wavelength=408*10^-9;
% For 408 nm light:
% nsno2=2.145+j*0.033;
% nalq3=1.85+j*0.15;

nsno2=2.145+j*0.033;
nalq3=1.85+j*0.15;

dmeas=[50 100 225 450 500 700 800 900 950 1150 1300]*10^-10; % m
Tmeas=[0.8151 0.75441 0.69828 0.66045 0.68166 0.75428 0.7823
 0.74769 0.74413 0.64987 0.6213];
%
% %% at 700 A:
% Tmeas=[75.428 79.102 79.069 79.105 79.269 79.589]/100;
% pcts=[0 2 4 6 8 10];
%
% %% from changing k by hand
% sno2n=[2.145];
% sno2k=[0.033 0.0048 0.005 0.0048 0.0038 0.002];

% For 0, 3 (using 2), and 6 (so 2, 6 same) at 300 A:
% 0pct >> aalq3(6)
%
% ans =
%
```

```
%     0.0259
% 3 (2), 6 pcts>> aalq3(6)
%
% ans =
%
%     0.0260

% Predicted reflectance at Alq3/Sno2 interface:
% 0pct>> rsno2(6)
%
% ans =
%
%     0.0623
% 3 (2) pct>> rsno2(6)
%
% ans =
%
%     0.0646
% 6pct >> rsno2(6)
%
% ans =
%
%     0.0653

% dmeas=dmeas*1.148; % correction of tooling factor from ellipsometry?

% Borosilicate (BK7) Sellmeier Equation
% (http://www.u-optic.com/material.htm)
B1=1.03961212;
B2=2.31792344*10^-1;
B3=1.01046945;
C1=6.00069867*10^-3; % um2
C2=2.00179144*10^-2; % um2
C3=1.03560653*10^2; % um2

% Constants:
mu0=4*pi*10^-7; % H/m, assuming constant throughout
eps0=8.854*10^-12; % F/m


% Tin Oxide Thicknesses
dsno2=[50:50:1300]*10^-10;

sno2H=zeros(length(dsno2), dsno2(end)*10^10+1, length(wavelength));
sno2E=zeros(length(dsno2), dsno2(end)*10^10+1, length(wavelength));
sno2I=zeros(length(dsno2), dsno2(end)*10^10+1, length(wavelength));
sno2Iend=dsno2(end)*10^10+1;
```

```
r=0;
t=0;

for i=1:length(wavelength)
    lambda=wavelength(i)

    lum=lambda*10^6;
    nBK7=sqrt(1+B1*lum.^2./(lum.^2-C1)+...
        B2*lum.^2./(lum.^2-C2)+...
        B3*lum.^2./(lum.^2-C3));

    % Measurement Parameters:
    k0=2*pi/lambda;

    epsGlass=eps0*(nBK7)^2;
    kGlass=k0*sqrt(epsGlass/eps0);
    glassvar=[0:2*pi/10:2*pi]/kGlass;

    % Layer 0 (air) to 1 (Alq3):
    k1=k0*nalq3;
    p01=k1./k0;
    d1=100*10^-10; % m, 100 Angstroms of Alq3
    d1div=[0:d1/100:d1];

    rho01=(1-p01)./(1+p01);
    tau01=2./(1+p01);

    T01=(1/tau01)*[1 rho01; rho01 1];

    % Layer 1 Propagation:
    T1=[exp(-j*k1*d1) 0; 0 exp(j*k1*d1)];

    % Layer 1 (Alq3) to 2 (SnO2):
    k2=k0*nsno2;
    p12=k2./k1;

    rho12=(1-p12)./(1+p12);
    tau12=2./(1+p12);

    T12=(1/tau12)*[1 rho12; rho12 1];

    % Layer 2 (SnO2) to 3 (Glass):
    k3=k0*nBK7;
    p23=k3./k2;
    d3=10^-9; % m % these are being averaged out
```

```
rho23=(1-p23)./(1+p23);
tau23=2./(1+p23);

T23=(1/tau23)*[1 rho23; rho23 1];

% Layer 3 (Glass) to 4 (air):
k4=k0;
p34=k4./k3;

rho34=(1-p34)./(1+p34);
tau34=2./(1+p34);

T34=(1/tau34)*[1 rho34; rho34 1];

for h=1:length(dsno2)
    d2=dsno2(h);
    d2div=[0:10^-10:d2];

    % Layer 2 Propagation:
    T2=[exp(-j*k2*d2) 0; 0 exp(j*k2*d2)];

    sumr=0;
    sumt=0;

    sumaalq3=0;
    sumasno2=0;
    sumaglass=0;

    p30=k3./k0;
    p20=k2./k0;
    p10=k1./k0;

    sumalq3I=0;
    sumsno2I=0;

    sumEalq3=0;
    sumEsno2=0;

    sumHalq3=0;
    sumHsno2=0;

    sumrsno2=0;

    for q=1:length(glassvar)
        beta=d3+glassvar(q);
        T3=[exp(-j*kGlass*d3) 0; 0 exp(j*kGlass*beta)];
```

```
E=zeros(2,8);

% Back face of glass is dephased, so just assume its a
% boundary.  Therefore, no propagation matrix.
E(:,8)=[1;0];
E(:,7)=T34*E(:,8);
E(:,6)=T3*E(:,7);
E(:,5)=T23*E(:,6);
E(:,4)=T2*E(:,5);
E(:,3)=T12*E(:,4);
E(:,2)=T1*E(:,3);
E(:,1)=T01*E(:,2);

R=E(2,1)/E(1,1);
T=1/E(1,1);

sumr=sumr+R*conj(R);
sumt=sumt+T*conj(T);

% Reflection at Alq3, Sno2 interface
sumrsno2=sumrsno2+(E(2,3)/E(1,3))*conj(E(2,3)/E(1,3));

% For forward traveling Poynting vector:
Iinit=E(1,1)*conj(E(1,1));
Iref=-E(2,1)*conj(E(2,1))/Iinit;
Iglassp=p30*E(1,6)*conj(E(1,6))/(Iinit);
Iglassm=-p30*E(2,6)*conj(E(2,6))/(Iinit);
Iout=1/Iinit;

% Although E/H can be deconstructed into forward and reverse
% traveling waves, S must be calculated from total E and H, or
% the standing wave components must be explicitly included.
Esno2=exp(-j*k2*d2div)*E(1,5)+exp(j*k2*d2div)*E(2,5);
Hsno2=p20*exp(-j*k2*d2div)*E(1,5)-p20*exp(j*k2*d2div)*E(2,5);
Isno2=Esno2.*conj(Hsno2)/Iinit;
sumsno2I=sumsno2I+Isno2;

Ealq3=exp(-j*k1*d1div)*E(1,3)+exp(j*k1*d1div)*E(2,3);
Halq3=p10*exp(-j*k1*d1div)*E(1,3)-p10*exp(j*k1*d1div)*E(2,3);
Ialq3=Ealq3.*conj(Halq3)/Iinit;
sumalq3I=sumalq3I+Ialq3;

sumaalq3=sumaalq3+1+Iref-real(Ialq3(1));
sumasno2=sumasno2+real(Isno2(end))-Iglassp-Iglassm;
% Sanity check:
sumaglass=sumaglass+Iglassp+Iglassm-Iout;
```

```
            % E-fields:
            sumEalq3=sumEalq3+Ealq3/Iinit;
            sumEsno2=sumEsno2+Esno2/Iinit;

            % H-fields:
            sumHalq3=sumHalq3+Halq3/Iinit;
            sumHsno2=sumHsno2+Hsno2/Iinit;

        end

        sno2I(h, sno2Iend-length(sumsno2I)+1:sno2Iend, i)
=sumsno2I/length(glassvar);
        alq3I(h,:,i)=sumalq3I/length(glassvar);

        sno2E(h, sno2Iend-length(sumsno2I)+1:sno2Iend, i)
=sumEsno2/length(glassvar);
        alq3E(h,:,i)=sumEalq3/length(glassvar);

        sno2H(h, sno2Iend-length(sumsno2I)+1:sno2Iend, i)
=sumHsno2/length(glassvar);
        alq3H(h,:,i)=sumHalq3/length(glassvar);

        r(h,i)=sumr/length(glassvar);
        t(h,i)=sumt/length(glassvar);
        aglass(h,i)=sumaglass/length(glassvar);
        aalq3(h,i)=sumaalq3/length(glassvar);
        asno2(h,i)=sumasno2/length(glassvar);

        rsno2(h,i)=sumrsno2/length(glassvar);
    end
end

% Assemble Profiles of E-fields in structure:
Efield=zeros(length(dsno2), 101+dsno2(end)*10^10, length(wavelength));
Efieldend=dsno2(end)*10^10+101;

dstruct=[0:1:(100+dsno2(end)*10^10)]*10^-10; % m

for i=1:length(wavelength)
    for h=1:length(dsno2)

        Efield(h, Efieldend-101+1:Efieldend, i)=alq3E(h,:,i);
        Efield(h, 1:Efieldend-101+1, i)=sno2E(h,:,i);
    end
end

% Assemble Profiles of H-fields in structure:
```

```
Hfield=zeros(length(dsno2), 101+dsno2(end)*10^10, length(wavelength));
Hfieldend=dsno2(end)*10^10+101;

dstruct=[0:1:(100+dsno2(end)*10^10)]*10^-10; % m

for i=1:length(wavelength)
    for h=1:length(dsno2)

        Hfield(h, Hfieldend-101+1:Hfieldend, i)=alq3H(h,:,i);
        Hfield(h, 1:Efieldend-101+1, i)=sno2H(h,:,i);
    end
end

% Assemble Profiles of Poynting Vector in structure:
poynting=zeros(length(dsno2), 101+dsno2(end)*10^10, length(wavelength));
poyntingend=dsno2(end)*10^10+101;

for i=1:length(wavelength)
    for h=1:length(dsno2)

        poynting(h, poyntingend-101+1:poyntingend, i)=alq3I(h,:,i);
        poynting(h, 1:poyntingend-101+1, i)=sno2I(h,:,i);
    end
end
```

Appendix C

Numerical Solver

Matlab script for the main function main.m

```
function [best, leastError] = main(option)
    %set the number of diffusion length and energy transfer distance steps
    numdiff = 11;
    numleng = 10;

    %initial guess of the diffusion length and energy transfer distance,
    %given upper and lower bounds
    diffLeng = linspace(120, 128, numdiff);
    engLeng = linspace(0.1, 1, numleng);

    %initial guess of the emission intensity coefficient
    intensity = 0.001;

    %other variables used to keep track of the current state of compution
    options = optimset('LargeScale','off');
    cDiffLeng = 0;
    cEngLeng = 0;
    leastError = 200;
    best = zeros(1,3);
    startTime = clock;

    %experimental data
    thickness = [10 25 45 65 85 100 125 150 175 200 300 400 500 600 700];
%   Before optical correction
%   targetInt = [0 0 0.3469 1 2.095 2.461 4.76 6.309 9.338 12.64 23.419
 36.415 54.951 71.844 81.884];
%   After optical correction
    targetInt = [0 0 0.601 1.691 3.449 3.968 7.402 9.451 13.472 17.569
```

```
      28.494 40.719 60.155 81.518 100];

    %initialize theoretical intensity
    theoreInt = zeros(1, length(thickness));

    for j=1:numdiff
        for k = 1:numleng
    if (diffLeng(j) + engLeng(k) < 60)
continue
    elseif (diffLeng(j) + engLeng(k) > 350)
continue
    end
     cDiffLeng = diffLeng(j);
     cEngLeng = engLeng(k);
     theoreInt = calculateInt([cDiffLeng, cEngLeng], option);
     [int,fval,exitflag,output] = fminunc(@optInt, intensity, options);
     if fval < leastError
         best = [int, cDiffLeng, cEngLeng]
         disp(int*100)
         leastError = fval
         currentTime = clock;
         elapsed = timedim(etime(currentTime, startTime), 'sec', 'hms');
         disp(strcat('Total time elapsed', ' :', num2str(elapsed), ':'))
         dlmwrite('best.txt', [best, leastError, elapsed], 'newline',
 'unix');
            end
        end
    end

    dlmwrite('outputfile.txt', [best, leastError, 0], 'newline', 'unix');

    function error = optInt(intGuess)
        error = sum((targetInt - theoreInt*intGuess).^2);
    end
end
```

Matlab script for auxiliary function calculateInt.m

```
function trialInt = calculateInt(input, option)
    diffLeng = input(1);
    engTransDist = input(2);

    thickness = [10 25 45 65 85 100 125 150 175 200 300 400 500 600 700];
    trialInt = zeros(1,length(thickness));

    for i=1:length(thickness)
        trialInt(i) = calculateTotalExcitons(thickness(i), diffLeng,
```

```
 engTransDist, option);
    end
```

Matlab script for auxiliary function calculateTotalExcitons.m

```
function totalEmission = calculateTotalExcitons(thickness, diffLeng,
 engTransLeng, option)

%initialize solution. To avoid singularity at x = 0, set the lower bound
%to 0.01
solinit = bvpinit(linspace(0.05,thickness), @calinit);
xint = linspace(0.05,thickness);
sol = zeros(1,1);
alpha = 5.6e-4;

if (option == 1) %turn on both energy transfer and dissociation
    sol = bvp4c(@EngTrans, @excitonDissociation, solinit);
elseif (option == 2) %turn on energy transfer but no dissociation
    sol = bvp4c(@EngTrans, @noDissociation, solinit);
else %turn on dissociation only
    sol = bvp4c(@noEngTrans, @excitonDissociation, solinit);
end

Sxint = deval(sol,xint);
emission = zeros(1, length(xint));
for j=1:length(emission)
    emission(j) = Sxint(1,j) / (1 + engTransLeng^3/xint(j)^3);
end
totalEmission = sum(emission) * thickness / length(emission);

    function dydx = EngTrans(x, y)
        dydx = zeros(2,1);
        dydx(1) = y(2);
        dydx(2) = y(1) / diffLeng^2 * (1 + engTransLeng^3/x^3) - 1;
%       dydx(2) = y(1) / diffLeng^2 * (1 + engTransLeng^3/x^3)
%  - exp(-alpha*(thickness-x));
    end

    function dydx = noEngTrans(x,y)
        dydx = zeros(2,1);
        dydx(1) = y(2);
        dydx(2) = y(1) / diffLeng^2 - 1;
    end

    function res = excitonDissociation(ya, yb)
        % want N(0) = 0 and dN/dx (at air/organic interface) = 0
        res = zeros(2,1);
```

```
        res(1) = ya(1);
        res(2) = yb(2);
    end

    function res = noDissociation(ya, yb)
        % want dN/dx (at x = 0) = dN/dx (at air/organic interface) = 0
        res = zeros(2,1);
        res(1) = ya(2);
        res(2) = yb(2);
    end

    function yinit = calinit(x)
        yinit = zeros(2,1);
        yinit(1) = (1 - cosh((x-thickness)/136)/cosh(thickness/136));
        yinit(2) = -sinh((x - thickness)/136)/cosh(thickness/136)/136;
    end
end
```

Appendix D

Monte Carlo Simulation for Time-resolved Photoluminescence

Matlab script for the main control function main.m

```
clear all;

thickness = linspace(10, 400, 40); % unit: A
nExcitons = 20000; % Number of excitons
batch = 100;
%absorption = 5.64e-4; % unit: / A
timeLimit = 100; % unit: nsec
decayTime = 17.4; % unit: nsec
unitTime = 0.01; % unit: nsec
energyTransDist = 10; % unit: A
maxDist = 1.897; % unit: A
nTimeInt = timeLimit / unitTime;

counts = unitTime:unitTime:timeLimit;

for n = 1:length(thickness)
    counts = [counts; decaySim2(thickness(n), nTimeInt, nExcitons, batch,
     timeLimit, decayTime, unitTime, maxDist, energyTransDist)];
end

name = input('Output file name: ', 's');
dlmwrite(name, counts', 'newline', 'unix');
```

Matlab script for auxiliary function decaySim2.m

```
function result = decaySim2(thickness, nTimeInt, nExcitons, batch,
timeLimit, decayTime, unitTime, maxDist, energyTransDist)

    nExcPerBatch = nExcitons / batch;
    result = zeros(1, nTimeInt);
    film = num2str(thickness);

    for b = 1:batch
        for n = 1:nExcPerBatch
            %temp = exp(-thickness * absorption);
            %position = -1/absorption*log(rand * (1 - temp) + temp);
            %assume uniform exciton generation
            position = rand*thickness; %initialize position

            for t = 1:nTimeInt
                breakNow = 0;
                decay = decayTime/(1 + (energyTransDist/position)^3);
                survival = exp(-unitTime/decay);

                if (rand > survival)
                    emit = 1 / (1 + (energyTransDist/position)^3);
                    if (rand < emit)
                        result(t) = result(t) + 1;
                    end
                    break
                else
                    position = position + normrnd(0,maxDist);
                end

                if (position > thickness)
                    position = 2 * thickness - position;
                end

                for pass=1:10
                    if (position < 0)
                        if (rand > 0)
                            position = -position;
                        else
                            breakNow = 1;
                            break
                        end
                    elseif (position > thickness)
                        position = 2*thickness - position;
                    else
                        break
                    end
                end
```

```
                if (breakNow > 0)
                    break
                end
            end
        end

        percent = num2str(b / batch * 100);
        disp(strcat(film, 'A', '::', percent, '% complete'))
    end
end
```

THIS PAGE INTENTIONALLY LEFT BLANK

Bibliography

[1] C. W. TANG and S. A. VANSLYKE, *Applied Physics Letters* **51**, 913 (1987).

[2] V. BULOVIĆ and Y. TISCHLER, Organic Opto-Electronics, MIT Course 6.789 Lecture and Recitation Notes, 2005.

[3] F. CACIALLI, *Philosophical Transactions: Mathematical, Physical and Engineering Sciences* **358**, 173 (2000).

[4] E. REICHMANIS, H. KATZ, C. KLOC, and A. MALIAKAL, *Bell Labs Technical Journal* **10**, 87 (2005).

[5] C. D. DIMITRAKOPOULOS and P. R. L. MALENFANT, *Advanced Materials* **14**, 99 (2002).

[6] T. W. KELLEY, P. F. BAUDE, C. GERLACH, D. E. ENDER, D. MUYRES, M. A. HAASE, D. E. VOGEL, and S. D. THEISS, *Chemistry of Materials* **16**, 4413 (2004).

[7] V. BULOVIĆ, P. E. BURROWS, and S. R. FORREST, *Semiconductors and Semimetals* **64**, 255 (2000).

[8] S. R. FORREST, *Organic Electronics* **4**, 45 (2003).

[9] J.-H. LEE, C.-I. WU, S.-W. LIU, C.-A. HUANG, and Y. CHANG, *Applied Physics Letters* **86**, 103506 (2005).

[10] J. G. EDEN, *Proceedings of the IEEE* **94**, 567 (2006).

[11] V.-E. CHOONG, Y. PARK, N. SHIVAPARAN, C. W. TANG, and Y. GAO, *Applied Physics Letters* **71**, 1005 (1997).

[12] Y. PARK, V.-E. CHOONG, B. R. HSIEH, C. W. TANG, and Y. GAO, *Physical Review Letters* **78**, 3955 (1997).

[13] R. R. CHANCE, A. PROCK, and R. SILBEY, *Journal of Chemical Physics* **62**, 2245 (1975).

[14] A. L. BURIN and M. A. RATNER, *Journal of Physical Chemistry A* **104**, 4704 (2000).

[15] Y. WU, Y. C. ZHOU, H. R. WU, Y. Q. ZHAN, J. ZHOU, S. T. ZHANG, J. M. ZHAO, Z. J. WANG, X. M. DING, and X. Y. HOU, *Applied Physics Letters* **87**, 044104 (2005).

[16] B. A. GREGG, J. SPRAGUE, and M. W. PETERSON, *Journal of Physical Chemistry B* **101**, 5362 (1997).

[17] A. MANI, J. SCHOONMAN, and A. GOOSSENS, *Journal of Physical Chemistry B* **109**, 4829 (2005).

[18] R. G. GORDON, *MRS Bulletin* **25**, 52 (2000).

[19] R. SNYDERS, M. WAUTELET, R. GOUTTEBARON, J. P. DAUCHOT, and M. HECQ, *Thin Solid Films* **423**, 125 (2003).

[20] S.-K. SONG, *Physical Review B* **60**, 11137 (1999).

[21] A. S. RYZHIKOV, R. B. VASILIEV, M. N. RUMYANTSEVA, L. I. RYABOVA, G. A. DOSOVITSKY, A. M. GILMUTDINOV, V. F. KOZLOVSKY, and A. M. GASKOV, *Materials Science and Engineering B* **96**, 268 (2002).

[22] B. J. INGRAM, G. B. GONZALEZ, D. R. KAMMLER, M. I. BERTONI, and T. O. MASON, *Journal of Electroceramics* **13**, 167 (2004).

[23] I. G. HILL and A. KAHN, *Journal of Applied Physics* **86**, 4515 (1999).

[24] M. D. HALLS and H. B. SCHLEGEL, *Chemistry of Materials* **13**, 2632 (2001).

[25] D. Z. GARBUZOV, V. BULOVIĆ, P. E. BURROWS, and S. R. FORREST, *Chemical Physics Letters* **249**, 433 (1996).

[26] H. MATTOUSSI, H. MURATA, C. D. MERRITT, Y. IIZUMI, J. KIDO, and Z. H. KAFAFI, *Journal of Applied Physics* **86**, 2642 (1999).

[27] V. BULOVIĆ, M. A. BALDO, and S. R. FORREST, Excitons and Energy Transfer in Doped Luminescent Molecular Organic Materials, in *Organic Electronic Materials: Conjugated Polymers and Low Molecular Weight Organic Solids*, edited by R. FARCHIONI and G. GROSSO, Springer Series in Materials Science, chapter 11, pp. 391–441, Springer-Verlag Berlin Heidelberg, Germany, first edition, 2001.

[28] A. C. ARANGO, A quantum dot heterojunction photodetector, Master's thesis, MIT, 2005.

[29] J. R. SHEATS, H. ANTONIADIS, M. HUESCHEN, W. LEONARD, J. MILLER, R. MOON, D. ROITMAN, and A. STOCKING, *Science* **273**, 884 (1996).

[30] R. PRIESTLEY, I. SOKOLIK, A. D. WALSER, C. W. TANG, and R. DORSINVILLE, *Synthetic Metals* **84**, 915 (1997).

[31] A. N. KRASNOV, *Applied Physics Letters* **80**, 3853 (2002).

[32] M. XU and J. XU, *Thin Solid Films* **491**, 317 (2005).

[33] M. D. GALANIN, *Luminescence of Molecules and Crystals*, chapter 1, Cambridge International Science Publishing, Cambridge, UK, 1996.

[34] L. J. VAN DER PAUW, *Philips Technical Review* **20**, 220 (1958/1959).

[35] M. SEGAL, private communication.

[36] M. POPE and C. E. SWENBERG, *Electronic Processes in Organic Crystals and Polymers*, chapter 1.D–F, pp. 39–134, Oxford University Press, Oxford, UK, second edition, 1999.

[37] V. M. AGRANOVICH, D. M. BASKO, G. C. LA ROCCA, and F. BASSANI, *Journal of Physics: Condensed Matter* **10**, 9369 (1998).

[38] V. G. PLEKHANOV, *Physical Review B* **54**, 3869 (1996).

[39] W. BENENSON, J. W. HARRIS, H. STOCKER, and H. LUTZ, *Handbook of Physics*, p. 347, Springer-Verlag, New York, New York, 2002.

[40] J. A. KONG, *Electromagnetic Wave Theory*, chapter 3.4, pp. 369–405, EMW Publishing, Cambridge, Massachusetts, 2005.

[41] M. A. BALDO and M. SEGAL, *Physica Status Solidi (a)* **201**, 1205 (2004).

[42] A. SUNA, *Physical Review B* **1**, 1716 (1970).

[43] M. A. BALDO, C. ADACHI, and S. R. FORREST, *Physical Review B* **62**, 10967 (2000).

[44] I. SOKOLIK, R. PRIESTLEY, A. D. WALSER, R. DORSINVILLE, and C. W. TANG, *Applied Physics Letters* **69**, 4168 (1996).

[45] C. F. MADIGAN and V. BULOVIĆ, *Physical Review Letters* **96**, 046404 (2006).

[46] G. D. SCHOLES, *Annual Review of Physical Chemistry* **54**, 57 (2003).

[47] D. L. DEXTER, *Journal of Chemical Physics* **21**, 836 (1953).

[48] H. BECKER, S. E. BURNS, and R. H. FRIEND, *Physical Review B* **56**, 1893 (1997).

[49] V.-E. CHOONG, Y. PARK, Y. GAO, M. G. MASON, and C. W. TANG, *Journal of Vacuum Science and Technology A* **16**, 1838 (1998).

[50] N. K. PATEL, S. CINÀ, and J. H. BURROUGHES, *IEEE Journal on Selected Topics in Quantum Electronics* **8**, 346 (2002).

[51] H. KUHN, *Journal of Chemical Physics* **53**, 101 (1970).

[52] H. KALLMANN, G. VAUBEL, and H. BAESSLER, *Physica Status Solidi (b)* **44**, 813 (1971).

[53] G. VAUBEL, H. BAESSLER, and D. MÖBIUS, *Chemical Physics Letters* **10**, 334 (1971).

[54] R. J. MARTÍN-PALMA and J. M. MARTÍNEZ-DUART, *Journal of Vacuum Science and Technologies A* **16**, 409 (1998).

[55] J. KALINOWSKI, V. FATTORI, and P. D. MARCO, *Chemical Physics* **266**, 85 (2001).

[56] C. F. MADIGAN, private communication.

[57] R. C. POWELL and Z. G. SOOS, *Journal of Luminescence* **11**, 1 (1975).

[58] V. M. KENKRE and Y. M. WONG, *Physical Review B* **22**, 5716 (1980).

[59] C. L. YANG, Z. K. TANG, W. K. GE, J. N. WANG, Z. L. ZHANG, and X. Y. JIAN, *Applied Physics Letters* **83**, 1737 (2003).

[60] P. PEUMANS, A. YAKIMOV, and S. R. FORREST, *Journal of Applied Physics* **93**, 3693 (2003).

[61] X. DU, Y. DU, and S. M. GEORGE, *Journal of Vacuum Science and Technologies A* **23**, 581 (2005).

[62] M. BENDER, W. SEELIG, C. DAUBE, H. FRANKENBERGER, B. OCKER, and J. STOLLENWERK, *Thin Solid Films* **326**, 72 (1998).

[63] H.-C. LEE and O. O. PARK, *Vacuum* **77**, 69 (2004).

[64] M. S. BRADLEY, Highly Absorptive Thin Films for Integrated Photonic Devices, Master's thesis, MIT, 2006.